



**HAL**  
open science

## The behaviour of a cloud ensemble in response to external forcings

Françoise M. Guichard, Jean-Luc Redelsperger, Jean-Philippe Lafore

► **To cite this version:**

Françoise M. Guichard, Jean-Luc Redelsperger, Jean-Philippe Lafore. The behaviour of a cloud ensemble in response to external forcings. Quarterly Journal of the Royal Meteorological Society, 1996, 122, pp.1043-1073. 10.1002/qj.49712253303 . meteo-00340114

**HAL Id: meteo-00340114**

**<https://meteofrance.hal.science/meteo-00340114v1>**

Submitted on 4 Nov 2024

**HAL** is a multi-disciplinary open access archive for the deposit and dissemination of scientific research documents, whether they are published or not. The documents may come from teaching and research institutions in France or abroad, or from public or private research centers.

L'archive ouverte pluridisciplinaire **HAL**, est destinée au dépôt et à la diffusion de documents scientifiques de niveau recherche, publiés ou non, émanant des établissements d'enseignement et de recherche français ou étrangers, des laboratoires publics ou privés.

# The behaviour of a cloud ensemble in response to external forcings

By F. GUICHARD\*, J.-L. REDELSPERGER and J.-P. LAFORE  
*Centre National de Recherches Météorologiques, France*

The behaviour of a population of tropical moderate precipitating clouds is investigated with a cloud-resolving model over a period equivalent to 2–3 days. The response of the system is analysed as a function of external forcings, comprising shortwave and longwave radiation, large-scale ascent effects and surface fluxes. Radiative and large-scale ascent processes enhance the convective activity. In all the experiments, an accumulation of humidity is observed in the upper part of the cloud layer and in the region above. In the case of weak large-scale ascent, a diurnal cycle of convection is found, having maximum activity during the night and minimum activity around noon. Depending on the anvil cloud coverage, a modulation of this cycle is found whose cause can be explained through an infrared radiative feedback. The anvil deck also has a diurnal cycle but phase shifted by six hours with reference to the convective cycle.

**KEYWORDS:** Cloud-resolving model Convection Radiative feedback Tropical precipitation

## 1. INTRODUCTION

Cloud processes have a major effect on the terrestrial climatic system. They have a dominant role in the radiative budget, directly through cloud radiative properties, and indirectly because convection is responsible for most of the vertical transport of water vapour, a very important greenhouse gas. Convection affects the large-scale circulation through the vertical redistribution of mass and momentum, sensible and latent heat.

Unfortunately, many cloud processes occur on temporal and spatial scales smaller than the grid spacing of general circulation models. Therefore, the large-scale effects of clouds have to be parametrized in these models, based on an assumption of scale separation.

Current parametrizations take into account an apparent heat source, Q1, and an apparent moisture sink, Q2, associated with cumulus convection. A large diversity of schemes exists, including some relatively simple ones (e.g. Kuo 1974) as well as schemes that rely on a much more physical basis (Arakawa and Schubert 1974). Parametrizations have been tested, validated and calibrated with the help of existing observational studies which diagnose the effects of cumulus convection on the large-scale environment (Yanai *et al.* 1973; Johnson 1984), and also, in a few cases, with the help of numerical simulations (Xu and Arakawa 1992). Cloud–radiation and cloud–surface interactions, as well as cumulus momentum transport, are still poorly represented, and there is a lack of consistency between the different cloud processes. For these reasons, the World Climate Research Programme has established a Cloud System Study (GCSS) as part of its GEWEX (Global Energy and Water Cycle Experiment), (Browning *et al.* 1993). Refer to Emanuel and Raymond (1993) for a review of the representation of cumulus convection in atmospheric models.

Climate studies are undertaken with the help of observations and general circulation models (GCMs) including complex 3-D models and also simplified 1-D vertical models (Betts and Ridgway 1989; Hu and Randall 1994; Satoh and Hayashi 1992). The last category allows one to isolate the convective component in climate and so to investigate several idealized scenarios. All these studies show that there is an important sensitivity to the treatment of convective subgrid processes (Arking 1991). Sensitivity to cloud schemes implies great uncertainties with regard to global warming induced by doubling atmospheric CO<sub>2</sub>. An inter-comparison of 19 GCMs (Cess *et al.* 1990) showed that important differences occurred, mainly through cloud feedbacks, with a global climate sensitivity parameter,  $\lambda$ ,

\* Corresponding author: Centre National de Recherches Météorologiques, (CNRS and Météo-France), 42 avenue de Coriolis, 31057 Toulouse Cedex, France.

that ranged from 0.39 to 1.23 K m<sup>2</sup> W<sup>-1</sup> ( $\lambda$  being the rate of change in global-mean surface temperature brought about by the global-mean direct radiative forcing).

Therefore, a better knowledge and understanding of moist convective processes are required so that the representation of these processes in large-scale models can be improved. This can be achieved with the help of observations and a two- or three-dimensional representation of convective systems. One approach is to use cloud resolving models (CRMs). These have been extensively developed during the past decade as computing power increased, and now include explicit treatment of a cloud ensemble, representing a useful tool for the better understanding of moist convective processes. From a beginning with the representation of an isolated cloud, the use of these models has been progressively extended to investigate cloud mesoscale systems and ensembles of clouds. A delicate problem arises from the fact that convection never acts alone, but in association with other processes such as surface fluxes, large-scale motions and radiation—processes possessing very different natures, space and time scales. For example, deep tropical convection often generates large stratiform anvil clouds which interact strongly with radiation. The radiative importance of this upper tropospheric stratiform cloudiness suggests that GCMs need to improve the link between cumulus convection and upper stratiform anvils.

The behaviour of a cloud population and some of its interactions with other processes has been documented in three different approaches based on CRMs.

First, several studies have explored the sensitivity of convection to external forcings in cases of shallow and deep convection. The sensitivity to large-scale effects has been documented by Soong and Ogura (1980), Tao and Soong (1986), Xu and Arakawa (1992), Xu *et al.* (1992) among others; this has made it possible partly to confirm the quasi-equilibrium hypothesis of Arakawa and Schubert (1974) despite there being frequently a mesoscale organization for the convection. Coupled radiation effects have also been introduced in mesoscale models (e.g. Wang *et al.* 1993). Tao *et al.* (1993) found an increase in precipitation ranging from 15 to 30% in cases of squall lines when longwave cooling was taken into consideration. Fu *et al.* (1995) go further in the analysis of convection–radiation interactions, and identify opposite mechanisms: an enhancement of convection by clear-sky cooling and a decrease in convection due to stratiform anvil clouds associated with deep convection. The impact of the diurnal cycle in radiation is discussed by Xu and Randall (1995). They find an early morning maximum of precipitation in the case of oceanic tropical convection.

The second approach focuses on the effects of convection on the large-scale fields. With a CRM for each simulated convective system it is possible to compute explicitly its global thermodynamical impact ( $Q_1$  and  $Q_2$ ) as well as the detail of the processes involved (latent heat release, vertical convective transports . . .). For example, this approach has clearly shown that deep convection modifies the vertical profiles of temperature and water vapour in different ways. That can be explained from the different convective vertical transports for temperature and water vapour (e.g. Gregory and Miller 1989; Lafore and Redelsperger 1991). In these studies, the significative contribution of rain evaporation to the determination of  $Q_1$  and  $Q_2$  also emphasizes the role of convective downdraughts, which cool and moisten the lower levels. This kind of approach can help to clarify the validity of the simplifications and hypothesis made in a parametrization.

Thirdly, the radiative convective equilibrium has been investigated with the help of 2-D simulations (Lau *et al.* 1993, 1994; Held *et al.* 1993; Sui *et al.* 1994). Until very recently this academic problem was treated with 1-D models (Betts and Ridgway 1989; Hu and Randall 1994; Satoh and Hayashi 1992). The interest of using a CRM is to obtain a better consistency between cloud processes, coupled to an explicit treatment of cloud–radiation and cloud–surface interactions. However, the feedback on the large-scale circulation is

not represented, and the large-scale motion must be prescribed. These authors compared the statistical equilibrium responses of their system to different values of sea surface temperature. They considered cases of deep convection over a period of several weeks. A frequent result was an increase of water vapour throughout the troposphere in response to surface warming, corresponding to the same behaviour as obtained in GCMs.

Following all these approaches, this study focuses on the behaviour of a population of clouds simulated with a CRM. The response to external forcings (large-scale ascent, surface fluxes and radiative processes) of moderate precipitating convection in an oceanic tropical environment is studied, as well as the sensitivity to these forcings. Nine numerical experiments with various large-scale forcings are presented. The cloud size is a few kilometres both horizontally and vertically, in this case of moderate convection, interactions with large-scale circulations are expected to be less important than for deep convective systems. Moreover, these cloud types have not been previously much studied. The simulations last for the equivalent of 2 to 3 days. This duration corresponds to a timescale which is typical for this kind of cloud population—much larger than the lifetimes of individual clouds which are of the order of a few hours. The system is simulated using the 2-D version of the CRM developed by Redelsperger and Sommeria (1986). Interactive radiative effects are introduced and are computed using the radiation model of the European Centre for Medium-Range Weather Forecasts (ECMWF) (Morcrette 1991).

The contents of this paper have been arranged as follows. The model and budget equations are presented in section 2. The various initial conditions of the simulations are summarized in section 3. By the use of the thermodynamical budgets, the evolution of the system is analysed in the case where external forcings are approximately in balance. In this way we can assess the relative importance of the different processes involved and understand why the system reaches or does not reach equilibrium (section 4). The sensitivity of the response of the cloud ensemble to external processes is then investigated in section 5. The influence of the diurnal cycle is dealt with in section 6.

## 2. THE MODEL

### (a) *The cloud-resolving model*

The non-hydrostatic cloud model of Redelsperger and Sommeria (1986) is the one used in this study. This model has been applied extensively over a large range of scales to represent squall lines, frontal systems and shallow convection. It includes prognostic equations for the three components of momentum with a diagnostic equation for the pressure, prognostic equations for the potential temperature,  $\theta$ , and for three states of water: water vapour, cloud droplets and raindrops. The ice-phase scheme of Caniaux *et al.* (1994) does not appear in the present study for the sake of simplicity, because we have focused mainly on moderate convection, associated with clouds which do not reach up to the high troposphere. A Kessler-type parametrization is used for microphysical processes, except for subgrid-scale condensation and the conversion from cloud droplets into raindrops (Redelsperger and Sommeria 1986). Special care has been given to the formulation of parametrized turbulent processes. Significant improvements over the usual methods have been achieved by taking advantage of previous developments validated in boundary-layer models. This parametrization incorporates the effect of thermal stratification and includes a prognostic equation for subgrid turbulent kinetic energy. For all the simulations, surface fluxes are assumed constant (additional simulations with parametrized surface fluxes – following Louis 1979 – have led to similar results, on a timescale of 2 to 3 days).

To represent cloud-radiative feedbacks properly, major efforts have been made to improve the existing long-wave radiation scheme (Redelsperger and Clark 1990). The

complete radiative model of the ECMWF (Morcrette 1991) has been tried, after modifications taking into account the specificity of the CRM. The radiative model computes the heating/cooling rates in the solar and long-wave spectra for a vertical column, in clear and cloudy conditions, taking into account the effects of gas, aerosols and hydrometeors. In particular, the cloud model provides the radiation scheme with temperature and water-vapour vertical profiles and also with prognostic liquid water contents that are then used for the calculations of cloud radiative properties. A brief description of this model, with details of its implementation is given in the appendix.

### (b) Budget equations

Our approach is based on the examination of the budgets of prognostic variables. This approach, introduced for boundary-layer clouds (e.g. Sommeria 1976), allows us to understand the different physical phenomena occurring in the cloud system and to infer the effects of cloud activity on the large-scale environment. In the present study, the budgets of the potential temperature,  $\theta$ , specific humidity,  $q_v$ , and specific contents of cloud droplets,  $q_c$ , and raindrops,  $q_r$ , are computed and analysed. Horizontal and time averages of the prognostic equations for these quantities lead to vertical one-dimensional equations. Vertical integration of these 1-D equations from the surface to the top of the cloud layer, leads to single-value budgets.

In our case, horizontal advection terms vanish when horizontally averaged over the domain, because of the cyclic lateral boundary conditions. The formulation of the budgets then proceeds as follows:

(i) *One-dimensional budgets.* The following equations apply:

$$\langle \pi \rangle \frac{\partial \tilde{\theta}}{\partial t} = - \frac{\langle \pi \rangle}{\langle \rho \rangle} \frac{\partial}{\partial z} (\langle \rho \rangle \tilde{w} \tilde{\theta}) + \frac{\langle L_v \rangle}{c_p} \tilde{Q} + \tilde{Q}_R + \langle \pi \rangle \left( \frac{\partial \tilde{\theta}}{\partial t} \right)_{LS} \quad (1)$$

$$\frac{\langle L_v \rangle}{c_p} \frac{\partial \tilde{q}_v}{\partial t} = - \frac{\langle L_v \rangle}{c_p \langle \rho \rangle} \frac{\partial}{\partial z} (\langle \rho \rangle \tilde{w} \tilde{q}_v) - \frac{\langle L_v \rangle}{c_p} \tilde{Q} + \frac{\langle L_v \rangle}{c_p} \left( \frac{\partial \tilde{q}_v}{\partial t} \right)_{LS} \quad (2)$$

$$\frac{\partial \tilde{q}_c}{\partial t} = - \frac{1}{\langle \rho \rangle} \frac{\partial}{\partial z} (\langle \rho \rangle \tilde{w} \tilde{q}_c) + \tilde{c} + \tilde{e}_c - \tilde{a} - \tilde{a}c + \left( \frac{\partial \tilde{q}_c}{\partial t} \right)_{LS} \quad (3)$$

$$\frac{\partial \tilde{q}_r}{\partial t} = - \frac{1}{\langle \rho \rangle} \frac{\partial}{\partial z} (\langle \rho \rangle \tilde{w} \tilde{q}_r) - \frac{1}{\langle \rho \rangle} \frac{\partial}{\partial z} (\langle \rho \rangle \tilde{V}_t \tilde{q}_r) + \tilde{e}_r + \tilde{a} + \tilde{a}c + \left( \frac{\partial \tilde{q}_r}{\partial t} \right)_{LS} \quad (4)$$

In these equations, for each of the variables  $\theta$ ,  $q_v$ ,  $q_c$  and  $q_r$ , which we shall represent by  $\alpha$ ,  $\langle \alpha \rangle$  and  $\tilde{\alpha}$  are the spatial (horizontal) average and the spatio-time average, respectively, such that

$$\tilde{\alpha} = \int_T \int_{L_x} \alpha \, dx \, dt = \int_T \langle \alpha \rangle \, dt,$$

where  $T$  is the average time period,  $L_x$  the horizontal dimension of the domain,  $\rho$  the density,  $L_v$  the latent heat, and  $\pi = T/\theta$ , the Exner function.

The first term on the right-hand side of these equations corresponds to the sum of the mean and turbulent advectons, and includes the surface fluxes given in the first layer of the model. The net condensation rate  $Q$  is the sum of the condensation of water vapour,  $c$ , the evaporation of cloud droplets,  $e_c$ , and raindrops,  $e_r$ . The term  $Q_R$  is the net radiative heating rate (solar and infrared). The terms  $a$  and  $ac$  correspond to the transformation of cloud droplets into raindrops by the processes of auto-conversion and accretion, respectively. The term

$$\frac{1}{\langle \rho \rangle} \frac{\partial}{\partial z} (\langle \rho \rangle V_t q_r)$$

represents sedimentation, where  $V_t$  stands for the terminal velocity of falling raindrops.

Following Sommeria (1976), large-scale effects are introduced through a large-scale vertical velocity  $W_{LS}$ . The term  $(\partial\alpha/\partial t)_{LS}$  denotes the change in  $\alpha$  due to this large-scale circulation, with

$$\left(\frac{\partial\alpha}{\partial t}\right)_{LS} = -W_{LS} \left(\frac{\partial\langle\alpha\rangle}{\partial z}\right).$$

In the present study, no large-scale horizontal transport has been introduced.

(ii) *Zero-dimensional budgets.* Vertical integration of the previous equations, putting  $\bar{\alpha} = \int_0^H c_p \langle\rho\rangle \bar{\alpha} dz$ , ( $H$  is the top of the cloudy layer), leads to the equations

$$\frac{d\bar{s}}{dt} = \Phi_s + \overline{\langle L_v \rangle Q} + \overline{c_p Q_R} + \left(\frac{d\bar{s}}{dt}\right)_{LS} \quad (5)$$

$$\frac{d\overline{\langle L_v \rangle q_v}}{dt} = \Phi_l - \overline{\langle L_v \rangle Q} + \left(\frac{d\overline{\langle L_v \rangle q_v}}{dt}\right)_{LS} \quad (6)$$

$$\frac{d\bar{q}_c}{dt} = \bar{c} + \bar{e}_c - \bar{a} - \bar{a}c + \left(\frac{d\bar{q}_c}{dt}\right)_{LS} \quad (7)$$

$$\frac{d\bar{q}_r}{dt} = \bar{e}_r + \bar{a} + \bar{a}c + Pr + \left(\frac{d\bar{q}_r}{dt}\right)_{LS}. \quad (8)$$

In Eqs. (5) and (6),  $s = c_p \langle\pi\rangle\theta + gz$  is the dry static energy. We shall also use the moist static energy  $h = s + \langle L_v \rangle q_v$ . In the present case, the vertical integration of the potential energy  $gz$  gives a constant ( $d\bar{g}z/dt = 0$ ). The vertical integration of advective terms leads to the turbulent surface fluxes  $\Phi_s$  and  $\Phi_l$ . Fluxes at the top of the layer were found to be negligible and for simplicity have not been included. Equations for cloud and rain water are similar to Eqs. (3) and (4), respectively, except that they do not have advective terms since there are no surface fluxes of liquid water. Vertical integration of the sedimentation term gives the surface precipitation rate  $P$ .

### (c) Discussion

On the right-hand side of Eqs. (5) and (6), one finds the four interacting components of the system: surface fluxes of sensible and latent heat,  $\Phi_s$  and  $\Phi_l$ , moist convection, radiation and large-scale effects, in that order (see also Fig. 1). The terms  $\bar{s}$  and  $\overline{\langle L_v \rangle q_v}$  are not affected in the same way in that there is no direct effect of radiation on water vapour, and  $\Phi_s \ll \Phi_l$  over the tropical ocean. In the present case of moderate convection, the large-scale ascent  $W_{LS}$  is moderate, nevertheless we shall see that each term is quantitatively important.

Changes in the vertical profiles of temperature and water vapour do not appear in the vertically integrated budgets. They correspond, nevertheless, to relevant information because the profiles of temperature and humidity control the level of convective instability, and so the convective activity.

The main features of the dynamical system are as follows. First, the ocean releases surface fluxes of latent and sensible heat at the bottom of the atmosphere. Moist convection is responsible for exchanges between sensible and latent heat through condensation/evaporation processes, and for a vertical redistribution of temperature and water vapour through advection.

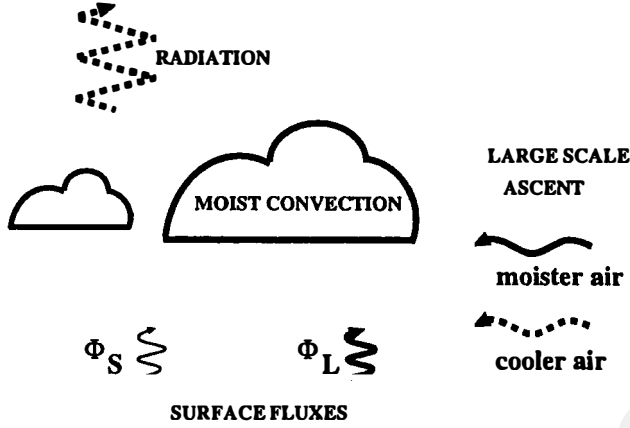


Figure 1. Schematic diagram showing the four interacting processes.

The apparent heat source  $Q_1$  and moisture sink  $Q_2$  defined in large-scale models for convection parametrization, can be estimated explicitly from Eqs. (1) and (2), and expressed in the form

$$Q_1 - \tilde{Q}_R = -\frac{\langle \pi \rangle}{\langle \rho \rangle} \frac{\partial}{\partial z} (\langle \rho \rangle \tilde{w} \theta) + \frac{\langle L_v \rangle}{c_p} \tilde{Q} \quad (9)$$

$$Q_2 = +\frac{\langle L_v \rangle}{c_p \langle \rho \rangle} \frac{\partial}{\partial z} (\langle \rho \rangle \tilde{w} \tilde{q}_v) + \frac{\langle L_v \rangle}{c_p} \tilde{Q}. \quad (10)$$

Radiative processes cool the troposphere at rates of 1–2 K d<sup>-1</sup> in clear-sky conditions. In cloudy conditions, these values are greatly affected (see the appendix), and for a cloud ensemble,  $\tilde{Q}_R$  is strongly controlled by the cloud fraction. The large-scale ascent brings colder and moister air into the system (warmer and drier air for a subsidence).

The difficulties involved in a study of this system arise from the fact that these four interacting processes possess very different natures, space and time scales.

The effects of moist convection occur on timescales much smaller than those of the other processes. The present model domain (horizontal size 120 km) allows the simultaneous presence of only 1 or 2 active convective clouds. Convective cells have a lifetime of about an hour, whereas  $W_{LS}$  and the surface conditions have much longer timescales, of the order of several hours for  $W_{LS}$  and several days, for surface conditions.

In the present study, we have analysed the behaviour of a cloud ensemble over a period of 2 to 3 days, with a prescribed constant  $W_{LS}$  and surface heat fluxes. It is important to notice that, over this timescale, the time variations of surface fluxes, radiation and large-scale ascent in Eqs. 5 and 6 are much smaller than those of the condensation latent heating, even if convection strongly modulates the spatial structure of these fields. This is particularly true if, as in the present case, the cloud fraction changes only slightly with time.

As convection does not directly affect the moist static energy,  $\bar{h}$ , of the system, a necessary condition for the system to reach equilibrium in terms of moist static energy is to have a balance between the three other processes. The radiative effect nevertheless depends on the cloud cover for short timescales, and, for the longer timescales, convection affects the large-scale fields; hence there are indirect effects from convection.

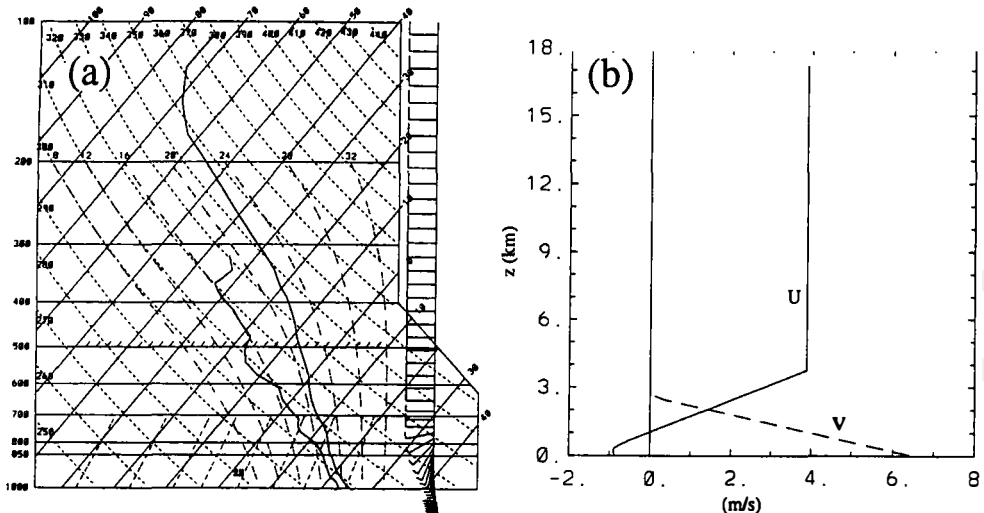


Figure 2. Initial vertical profiles: (a) skew- $T$  log- $P$  diagram; (b) wind components ( $\text{m s}^{-1}$ ).

### 3. EXPERIMENTAL CONDITIONS

In the present study we have focused on the case of moderate convection simulated in a 2-D framework. The model is initialized with a sounding, obtained from the GATE experiment, previously used by Balaji *et al.* (1993) and characteristic of the tropical oceanic environment. Two profile modifications have been introduced so as to be able to cater for the development of moderate convection. We altered the  $(\theta, q_v)$  profile slightly (Fig. 2(a)) to eliminate the inversion located at about 2 km. Also, the  $x$ -component of the wind,  $u$ , was modified to give a more moderate shear (Fig. 2(b)). A random perturbation of 0.2 K amplitude was introduced in the initial temperature field at the lowest level. The domain measured 120 by 17  $\text{km}^2$ . The horizontal grid length,  $\Delta x$ , was 800 m and the vertical grid length,  $\Delta z$ , ranged from 70 m near the surface to about 500 m above 12 km (55 vertical levels). A time-step of 7.5 seconds was used.

There are three different profiles of large-scale vertical velocity  $W$  (Fig. 3). The profile  $W_2$  is based on a pre-storm cluster-scale average of eight cases from GATE (Frank 1978). The profiles  $W_0$  and  $W_1$  are identical to  $W_2$ , except that the amplitude has been multiplied by 1/3 and 2/3, respectively. For all the experiments, an upper-level subsidence has been added with a maximum of  $1.1 \text{ cm s}^{-1}$  at 0.1 km (Fig. 3). The aim of this addition is to avoid deep convection and partly to balance radiation cooling. The radiation computation is made for 17 h LT, as at that time it corresponds approximately to the day-average short-wave radiative contribution.

Several experiments have been carried out and are summarized in Table 1. Experiment REF corresponds to the control simulation to be described in the following section. The aim of this simulation was to evaluate the behaviour of a cloud system under balanced external forcings. In this case, the smaller large-scale velocity has been used and the sensible and latent surface heat fluxes fixed at 7.5 and 75  $\text{W m}^2$ , respectively. Experiments FX, FXRAD and FXLS investigate the sensitivity of the system to the radiation and large-scale effects. Two additional experiments HIGHLS 1 and HIGHLS 2 document the sensitivity to the amplitude of the large-scale ascent. The sensitivity to the diurnal cycle is investigated in the experiments CYCLE, CYCLE 1 and CYCLE 2.

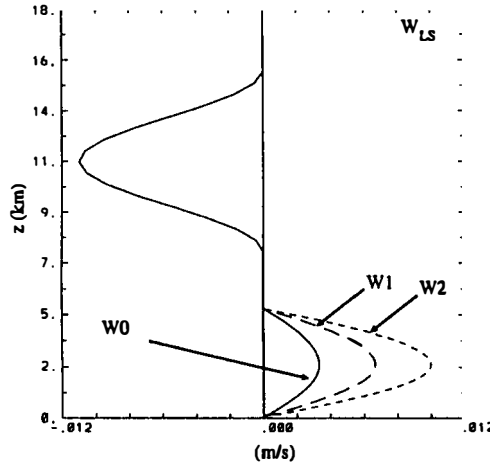


Figure 3. Large-scale ascent profiles.

TABLE 1. MAIN FEATURES OF THE EXPERIMENTS.

Experiments	Radiation	Large scale	Surface latent-heat fluxes, $\phi_1$ ( $\text{W m}^{-2}$ )
REF	fixed at 5.00 p.m.	$W_0$	75
FX	no	no	75
FXRAD	fixed at 5.00 p.m.	no	75
FXLS	no	$W_0$	75
HIGHLS 1	fixed at 5.00 p.m.	$W_1$	75
HIGHLS 2	fixed at 5.00 p.m.	$W_2$	75
CYCLE	diurnal cycle	$W_0$	75
CYCLE 1	diurnal cycle	$W_0$	50
CYCLE 2	diurnal cycle	$W_0$	100

In all experiments, surface sensible-heat fluxes  $\phi_s = 0.1 \phi_1$ .  $W_0$ ,  $W_1$  and  $W_2$  correspond to the different profiles reproduced in Fig. 3.

#### 4. THE CONTROL EXPERIMENT

##### (a) Basic features

In the control experiment REF, as in all the experiments, clouds of different shapes and sizes develop with a typical size of a few kilometres in both the  $x$  and  $z$  directions (Fig. 4). In the example given in the figure, several small clouds are present which have their bases located at about 400 m. Some, such as the two clouds located far in the east, will become active. In the west, a cloud in the decaying stage can be seen. Figure 5(a) shows the large time variability of the cloud layer. The base is quite stable but the top ranges from 4 km to about 11 km. An initial spin-up stage occurs lasting about three hours, corresponding to the time needed to organize the PBL (planetary boundary layer) and convection. After this period and during the first two days, there is a succession of well-defined stages, lasting a few hours, with the amounts of cloud water content,  $\tilde{q}_c$ , alternately high and low. During most of this time, these local maxima are due to only one or two active clouds. Cloud cover (not shown) reaches 15%, but remains of the order of a few per cent on average. After 48 h, a more severe convective event occurs with a large cloud which develops and extends up to 11 km, also extending horizontally over a few tens of kilometres. This event

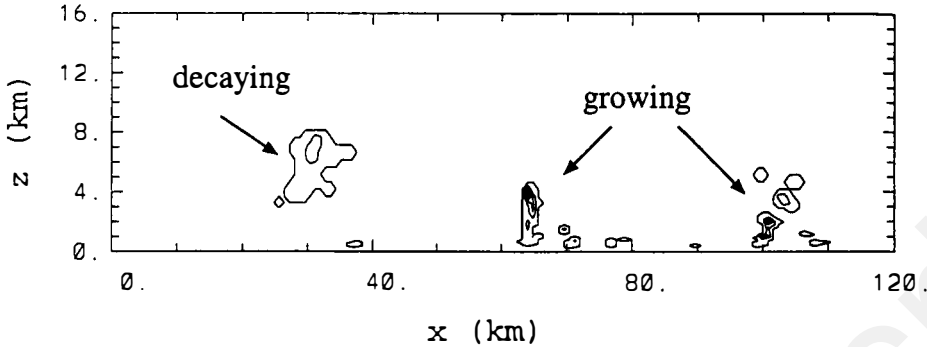


Figure 4. Vertical cross-sections of cloud field at 25 h 30 min for experiment REF.

lasts for about four hours. During the decay stage of this cloud, a high-level cloud deck persists, growing upwards and extending horizontally. This deck occupies as much as 70% of the domain horizontally during the final hours of the simulation. This important cloud coverage could be due partly to the cyclic lateral boundary conditions. Condensates are not allowed to be transported out of the domain. Under this deck, smaller clouds develop again on the third day, but their tops stay below 5–6 km.

The field of cloud water content,  $\tilde{q}_c$ , is well correlated with the net condensation/evaporation rate  $(\langle L_v \rangle / c_p) \tilde{Q}$  (Fig. 5(b)) and with the precipitation rate  $P$  (Fig. 5(c)). Local maxima of  $\tilde{q}_c$  correspond to local maxima in  $\tilde{Q}$ ; and peaks in  $P$  follow a few tens of minutes later. Maxima in condensation are associated with strong evaporation rates of cloud droplets,  $\tilde{e}_c$ , at the top of the cloud layer and of raindrops,  $\tilde{e}_r$ , under it (Fig. 5(b)). The absolute intensity of this evaporation is much smaller than for the condensation, but evaporation also occurs over a longer time.

### (b) Budgets

In this section, we analyse the thermodynamical budgets over the period  $T$  from 8 h to 48 h, corresponding to a rather homogeneous period that includes several convective events (Fig. 5). The first three hours of simulation correspond to a spin-up period followed by a stage between 3 h and 8 h during which convective activity increases, but is still weaker than after 8 h, with cloud tops remaining under 5 km. After 48 h the behaviour of the system is quite different and will be discussed at the end of this section. The vertical integration of the budget analysis concerns only the layer  $H$  from 0 to 8 km, since we have not considered the upper troposphere above the cloud layer.

(i) *Zero-dimensional budgets.* To analyse the system's behaviour on small timescales, Figs. 6(a), (b) and (c) present the evolution of the budgets of  $\bar{s}$  and  $\overline{\langle L_v \rangle q_v}$  over the period 8 h to 48 h. The latent heating,  $\overline{\langle L_v \rangle Q}$ , shows large variations with peaks that, locally, reach  $1000 \text{ W m}^{-2}$ . The time average is  $91 \text{ W m}^{-2}$  with a standard deviation of  $164 \text{ W m}^{-2}$ . The surface fluxes, radiation and large-scale effects stay roughly constant, with variations two orders of magnitude smaller (under  $15 \text{ W m}^{-2}$ ). The net radiation cooling, for example, slowly decreases from  $-114 \text{ W m}^{-2}$  at 8 h to  $-99 \text{ W m}^{-2}$  at 48 h, as the cloud cover increases. The net latent heating rate,  $\overline{Q}$ , thus plays the major part in controlling the large variability of  $\bar{s}$  and  $\langle L_v \rangle q_v$ , noted on the small timescales.

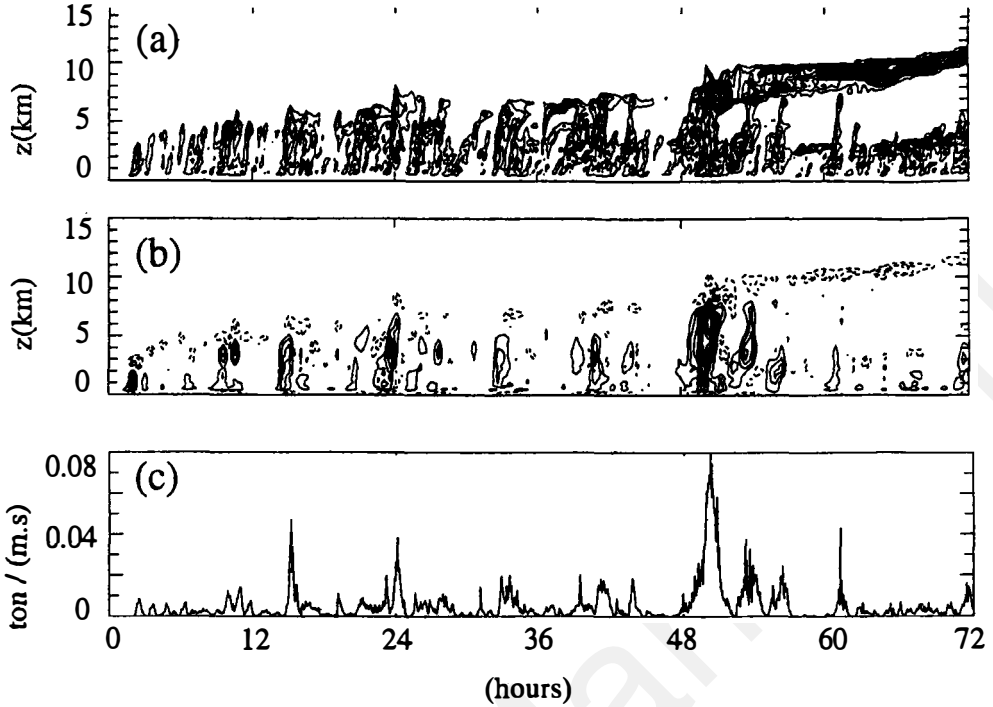


Figure 5. Evolution with time for experiment REF of: (a) average cloud water content  $\tilde{q}_c$  (kg kg<sup>-1</sup>); (b) net condensation rate  $((L_v)/c_p)\bar{Q}$ , (K s<sup>-1</sup>); (c) precipitation rate. Values of  $\tilde{q}_c$  are averaged over 10 min; the contour interval is  $10^{-5}$  (lower and higher contours are  $10^{-5}$  and  $15 \times 10^{-5}$ , respectively). Values of  $((L_v)/c_p)\bar{Q}$  are averaged over 30 min; the contour interval is  $5 \times 10^{-5}$  for positive values (continuous lines; lower and higher contours are  $5 \times 10^{-5}$  and  $5 \times 10^{-4}$ , respectively) and  $2.5 \times 10^{-5}$  for negative values (dotted lines; lower and higher contours are  $-1.25 \times 10^{-4}$  and  $-2.5 \times 10^{-5}$ , respectively).

As we are here more interested in studying the (non-) equilibrium of the system, the following budgets will be averaged over  $T$ , so that transient features due to convection are erased.

The time-mean budget of total moist static energy  $\bar{h}$  (Fig. 7(a)) shows that the system is approximately in balance when averaged over the period  $T$  and over the convective layer depth  $H$ . The gain of  $\bar{h}$  by surface fluxes ( $83 \text{ W m}^{-2}$ ) and the large-scale forcing ( $32 \text{ W m}^{-2}$ ) are to a first order ( $7 \text{ W m}^{-2}$ ) compensated for by the net radiative cooling ( $-108 \text{ W m}^{-2}$ ). This stresses the role of the large-scale forcings in allowing equilibrium, even on the scale of this domain. These external sources however are not redistributed by convection to give constant  $\bar{s}$  and  $(L_v)q_v$  (Figs. 7(b) and (c)). In fact, the atmosphere cools ( $-43 \text{ W m}^{-2}$ ) and moistens ( $+50 \text{ W m}^{-2}$ ). For the dry static energy,  $\bar{s}$ , each source is quantitatively important except for the surface fluxes which are one order smaller. All sources of  $(L_v)q_v$  are of equal magnitude. About two thirds of the water vapour introduced by surface fluxes and large-scale motion is condensed, and one third stored.

(ii) *Water budgets.* The processes changing  $q_c$  and  $q_r$  are in balance on the scale of the domain, as shown on the water-cycle budget (Fig. 8(a)) and on the behaviour vertically of these processes (Figs. 8(b) and (c)). This is the case in all experiments for time averages exceeding a few hours. In consequence, the time-mean net condensation,  $\bar{Q}$ , and precipi-

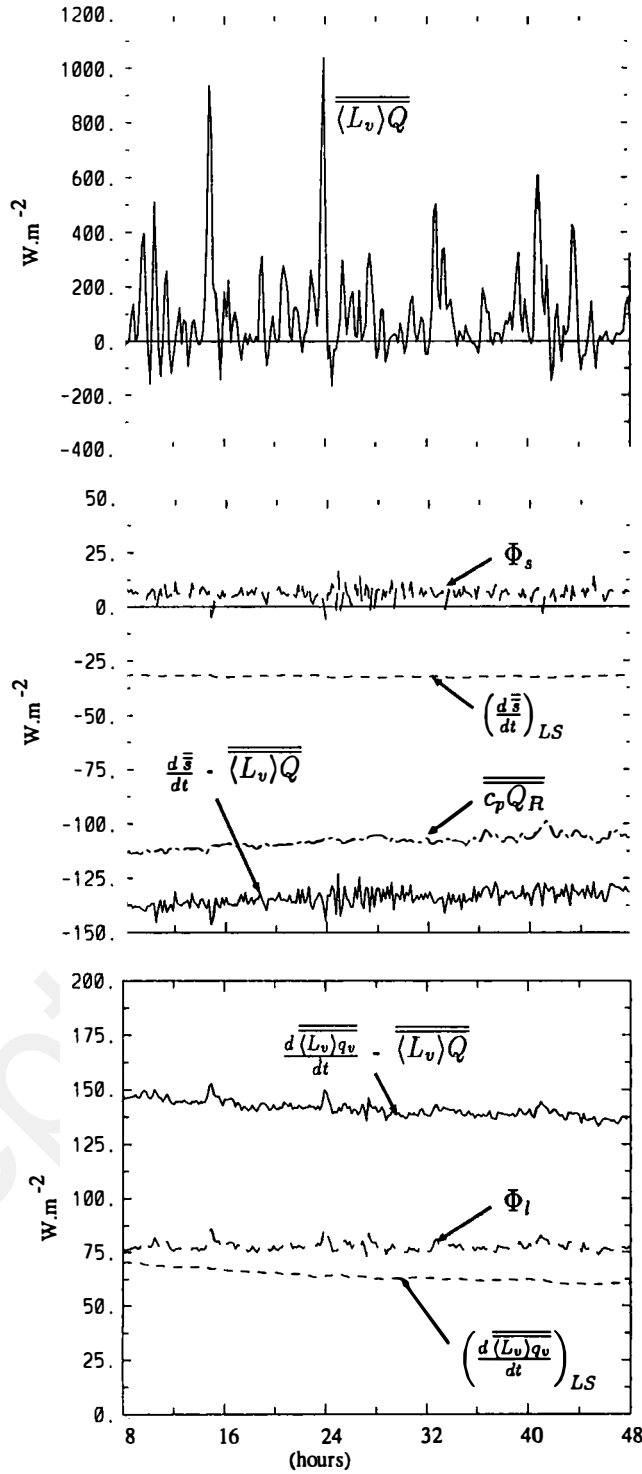


Figure 6. Evolution with time over the period 8 h to 48 h for experiment REF of: (a)  $\overline{\overline{(L_v)Q}}$ ; and, of the other terms of the budgets, of: (b)  $\overline{\overline{s}}$ ; (c)  $\overline{\overline{(L_v)q_v}}$ , with the time average  $T$  taken equal to 10 min (see text for definition).

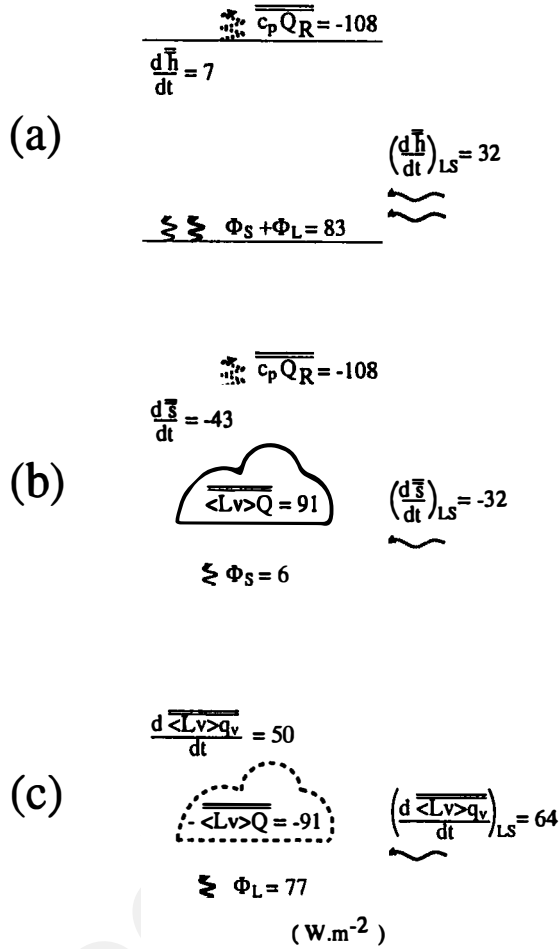


Figure 7. OD budgets averaged over the  $T$  period from 8 h to 48 h for experiment REF of: (a)  $\bar{h}$ ; (b)  $\bar{s}$ ; (c)  $\langle L_v \rangle q_v$ , (W m<sup>-2</sup>, as for all following OD budgets).

tation rates are balanced. Cloud droplet evaporation reduces the value of  $\bar{Q}$  considerably, in contrast to the rain evaporation which stays weak in this case of moderate convection. Water budgets done for deeper convective systems such as squall lines, using observations (Leary and Houze 1980; Chong and Hauser 1989) or simulations (Tao *et al.* 1993; Caniaux *et al.* 1994), gave similar results and, in particular, showed a high degree of consistency for all types of hydrometeor, which contrasts with the continuous increase in the total water vapour.

(iii) *One-dimensional budgets.* The corresponding distributions in the vertical of the temperature and moisture budgets are shown in Fig. 9. Two distinct layers appear: the subcloud layer from 0 to 0.4 km and the cloud layer from 0.4 km to 8 km. The resulting cooling previously noted is located mainly above 4.5 km in the upper part of the cloud layer. Between the surface and 4 km the cooling remains weak. In the subcloud layer, the evaporation of raindrops and the radiative cooling almost compensate for the vertical transport of potential temperature,  $\theta$ . In the cloud layer under 4.5 km,  $(\langle L_v \rangle / c_p) \bar{Q}$  is approximately equilibrated by radiative and large-scale effects. The vertical transport is

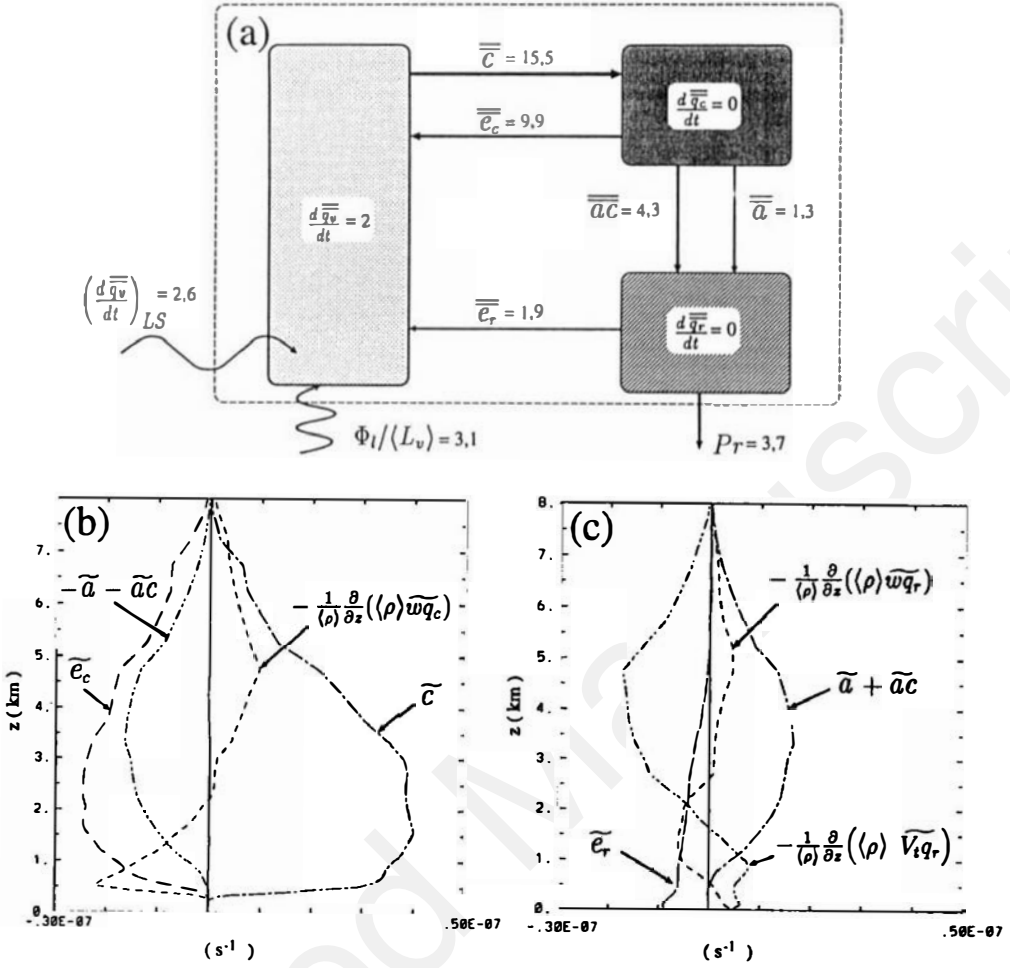


Figure 8. Water budgets averaged over the period from 8 h to 48 h for experiment REF: (a) the OD water-cycle budget, and the 1D budgets of (b)  $\bar{q}_c$  and (c)  $\bar{q}_r$ .

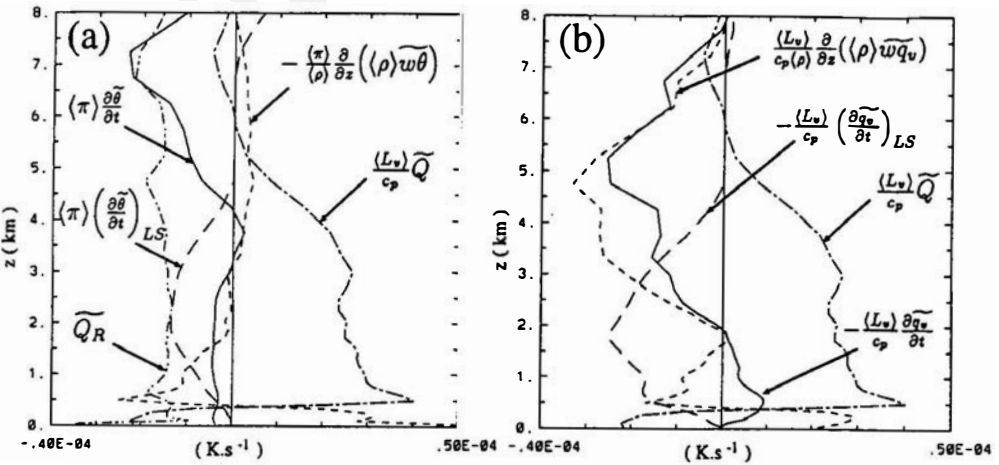


Figure 9. Vertical budgets averaged over the period from 8 h to 48 h for experiment REF of (a)  $\langle \pi \rangle \tilde{\theta}$ ; (b)  $-(L_v)/c_p \tilde{q}_v$ .

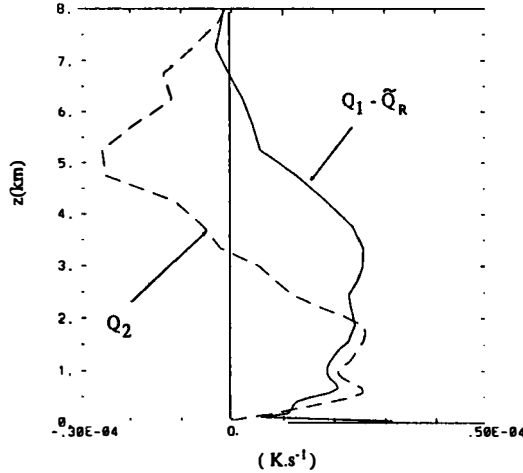


Figure 10. Vertical profiles of  $Q_1 - \widetilde{Q}_R$  and  $Q_2$  averaged over the period from 8 h to 48 h for experiment REF.

important only at the bottom of this layer and in the first two kilometres, corresponding to an upward flux of sensible heat. The cooling of the upper part of the cloud layer is due to radiative flux divergence.

In contrast with the previous case of cooling caused mainly by an unbalanced external forcing, the storage of water vapour localized between 2 and 8 km (i.e. in and above the cloud layer) is driven by the vertical transport. Convection acts continuously in the same way, i.e. in transporting water vapour upwards. In the present case, convection does not condense all the water vapour introduced. The decoupling between the distributions of  $\bar{\theta}$  and  $\bar{q}_v$  is caused by convective transport and radiation.

These above results indicate that, on the timescale of a day, the system is unable to equilibrate, in spite of there being no significant modification of  $\bar{h}$  by the three external forcings: radiation, large-scale motion and surface fluxes. The most noticeable point concerns water vapour storage and its redistribution in the vertical. This storage phenomenon was previously noticed by Gregory and Miller (1989) and Lipps and Hemler (1986) in simulations and observations of cases of deep convection. A water vapour storage amounting to 60–70% was found. In the present case, the vertical structure of this storage leads to a very significant decoupling of the profiles of  $(Q_1 - \widetilde{Q}_R)$  and  $Q_2$  above 2 km (Fig. 10); as already noted by Johnson (1984) for observations, and by Lafore *et al.* (1988) for simulations of squall-line systems. The decoupling seems to be a general feature, as it has also been detected for frontal system simulations by Redelsperger and Lafore (1994). It is possible that it may have an important impact on the vertical distribution of moisture, and consequently on radiative processes. As noted previously, no large-scale horizontal advection was imposed in our simulations. Although it is weaker than the large-scale vertical advection, its effect could weaken the vapour storage process. As shown by Soong and Tao (1980), large-scale transport can lead to low-level moistening and high-level drying, i.e. the opposite effect to the eddy transport of  $\bar{q}_v$ .

(iv) *Budgets for the third day of simulation.* The last day of simulation can be analysed by considering two different periods. Between 48 h and 58 h convection is much more intense than before, with a first peak of precipitation lasting about five hours followed

by two weaker peaks (Fig. 5). Over this period, convection eliminates more than twice the water vapour introduced over the same time (figure not shown). At 58 h all the water vapour introduced since 8 h has been eliminated. Over the last part of the experiment, from 58 h to 72 h, the clouds are localized in two distinct layers. For the lower layer, the main features of the convective activity are very similar to those found between 8 h and 48 h. In particular, there is an important storage of water vapour driven by advection in the upper part of this layer. Nevertheless, the deeper clouds in this layer reach up only to about 5 km. This is probably related to the stabilizing effect of the convection occurring between 48 h and 58 h, and further reinforced in the higher layers above by the radiative heating generated at the bottom of the high cloud deck.

The budget analysis over the period 8 h to 48 h suggests that during the first two days, moderate convection in the 0 to 6 km layer moistens and cools mid levels of the troposphere, which results in deeper convection on the third day. It stresses that the concept of equilibrium is valid only over the full depth of the troposphere and over a scale of several days. It also demonstrates the strong transient character of the convection.

## 5. SENSITIVITY TO EXTERNAL FORCINGS

The results of the control experiment REF have shown that the external forcings, i.e. surface fluxes, radiative processes and large-scale ascent, represent important contributions in the thermodynamical budgets. In this section, the sensitivity of the system to these forcings is investigated.

### (a) *Large-scale ascent and radiation*

The experiment FX includes only surface fluxes, FXRAD includes surface fluxes and radiation and FXLS includes surface fluxes and large-scale ascent. For these three experiments (Fig. 11) the cloud layer is weaker than in the control experiment REF (Fig. 5(a)). The cloud top remains below 8 km over the three days (Fig. 11), and no extreme event as in REF occurs after 48 h. From these figures we can see that the introduction of radiation and/or a large-scale ascent has an important impact on the simulated cloud field. The convective activity is particularly weak in the experiment FX, whereas experiments FXRAD and FXLS correspond to intermediate cases with longer periods of low activity than in experiment REF, such as the one observed between 18 and 30 h in FXLS. The evolution in time of the cumulative precipitation allows us to quantify this impact (Fig. 12). Experiments FX, FXRAD, FXLS and REF have mean slopes that become gradually larger and larger in spite of the existence of local peaks (at about 30 h and 40 h for FXLS and 30 h for FXRAD, for example). After 48 h, experiments FX, FXRAD and FXLS have produced, respectively, 28, 67 and 85 per cent of the total precipitation that was produced in experiment REF. Using the Arakawa–Schubert scheme and observed data from GATE phase III, Lord (1982) analysed the impact of various forcings on the convective activity. His results underlined the importance of the impact of large-scale advection of sensible heat on convective activity. He found a significant increase of precipitation due to the introduction of radiative processes, particularly in suppressed conditions. Miller and Frank (1993) developed an analogous sensitivity study based on simulations of a mesoscale convective system.

The time-mean budgets of the dry static energy,  $\bar{s}$ , and the difference between dry and moist static energies,  $\overline{\langle L_v \rangle q_v}$ , are presented in Fig. 13, for a time average over the period  $T$  from 8 h to 48 h. It should be noted that the large-scale forcings  $(\overline{ds/dt})_{LS}$  and

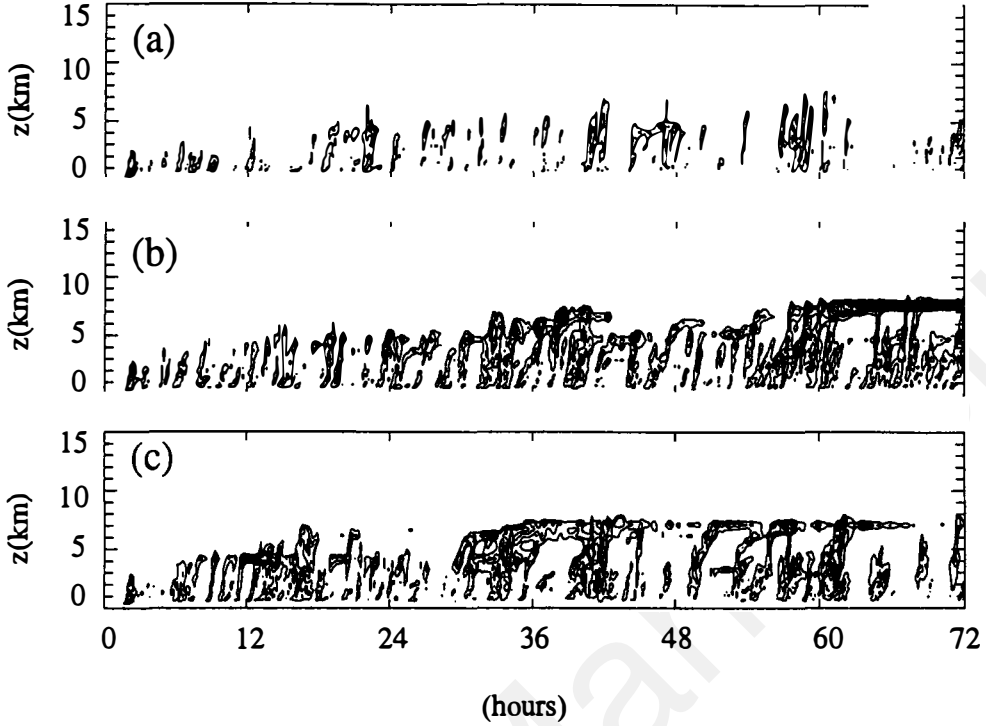


Figure 11. Same as Fig. 5(a), but for experiments (a) FX; (b) FXRAD; (c) FXLS. Values of  $\tilde{q}_c$  are averaged over 10 min, contour interval  $10^{-5}$ . The lower contour is  $10^{-5}$  and the higher contours are  $4 \times 10^{-5}$  for FX,  $11 \times 10^{-5}$  for FXRAD and  $7 \times 10^{-5}$  for FXLS.

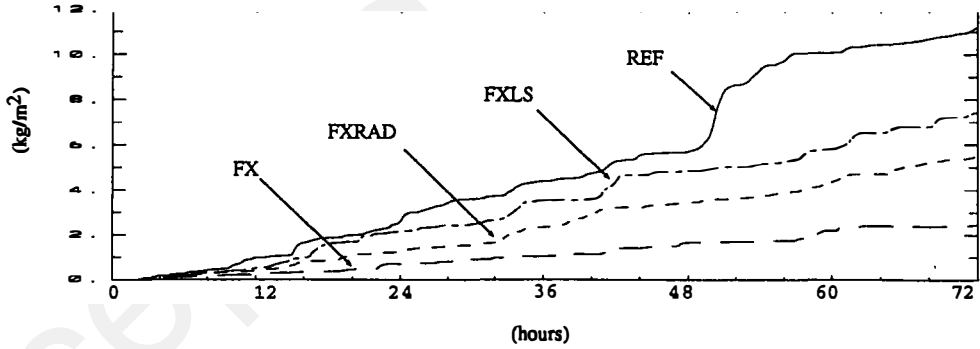


Figure 12. Cumulative precipitation for experiments REF, FX, FXRAD and FXLS.

$(d\langle L_v \rangle q_v / dt)_{LS}$  for the FX and FXRAD simulations, are not strictly zero, owing to the subsidence still being maintained above the cloud layer.

It appears from these budgets that the cloudy activity, as measured by  $\langle L_v \rangle \bar{Q}$ , is quite different as between the four experiments. The main difference is between FX and the other experiments, with values of  $\langle L_v \rangle \bar{Q}$  lower by a factor of 2 to 3 for FX. Both radiation and large-scale ascent enhance convection, but in a nonlinear way. Compared with FX, the introduction of radiation alone (FXRAD) increases the convective activity by a factor of 2,

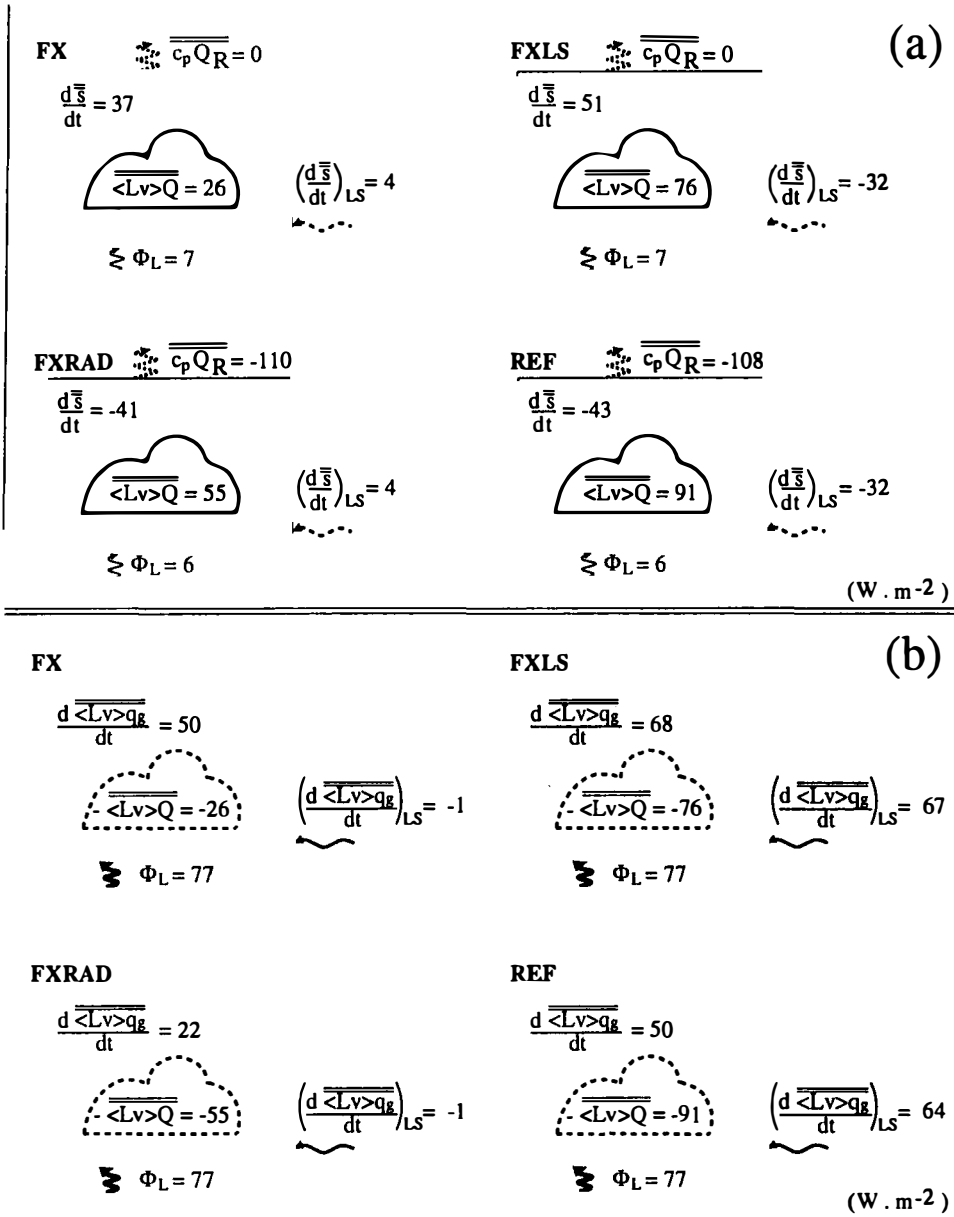


Figure 13. Budgets averaged over the period 8 h to 48 h for experiment REF, FX, FXRAD and FXLS of: (a)  $\overline{s}$ ; (b)  $\langle Lv \rangle q_v$ .

whereas the introduction of large-scale ascent alone (FXLS) increases it by a factor of 3. Finally, with both effects (REF), one obtains an increase by a factor of 3.5. A comparison of experiments FXLS and REF, both with a large-scale ascent, also indicates an enhancement of convection of about 20%, by radiative processes.

The impact of radiation is nevertheless different from the impact due to large-scale ascent. Radiation has a direct impact on the sensible heat budget only (the radiative cooling

takes values of about  $-110 \text{ W m}^{-2}$ ; see Fig. 13). It leads to a net cooling for experiments FXRAD and REF (of  $-41$  and  $-43 \text{ W m}^{-2}$ , respectively) despite the convective enhancement due to radiation. The latent-heat budget is affected by radiation through this convective enhancement. As a result, radiation is responsible for an indirect drying, and its introduction leads to  $-28$  and  $-18 \text{ W m}^{-2}$  additional drying for experiments FXRAD and REF, respectively.

A different effect is seen with the large-scale ascent which brings in cooler, but also moister, air that directly intensifies condensation. The introduction of the large-scale ascent leads, in both cases (compare FXLS with FX, and REF and FXRAD), to an increase of the net moistening, despite the enhancement of the convective activity. As a result, the sensible-heat budgets do not show any significant cooling, but instead a higher net heating for FXLS than for FX ( $51$  instead of  $37 \text{ W m}^{-2}$ ), and almost the same net cooling for FXRAD and REF.

Radiation and large-scale ascent thus have different impacts that partly compensate for each other when both processes are acting together as in experiment REF. It is especially true for moisture, for which the same degree of moistening ( $50 \text{ W m}^{-2}$ ) is obtained for experiments FX and REF, whereas in experiment FXRAD there is weak moistening ( $22 \text{ W m}^{-2}$ ) and in experiment FXLS strong moistening ( $68 \text{ W m}^{-2}$ ).

To analyse the specific impacts of radiation and large-scale ascent, it is useful to examine the vertical distribution of the diabatic source  $(\langle L_v \rangle / c_p) \bar{Q}$ , and the net drying  $-(\langle L_v \rangle / c_p) \partial \bar{q}_v / \partial t$  (Fig. 14).

So far as the diabatic source is concerned (Fig. 14(a)), the cloud layer in experiment FX is shallower than in the case of the other three. The major impact of the large-scale ascent is more obvious in the 1-D budgets. In particular, between 1 and 4 km, the large-scale introduction of cooler and moister air increases the values of  $\bar{Q}$ . The introduction of radiative processes increases the convective activity, particularly at the bottom of the cloud layer (compare FX with FXRAD, and FXLS with REF). Its impact in the cloud layer is particularly important for FXRAD compared to FX, although the minimum of  $\bar{Q}$  at 2.5 km, observed in experiment FX, still exists in FXRAD.

The vertical structure of the net drying (Fig. 14(b)) presents common features seen in the four simulations. In particular, the moisture storage is located in the upper part of the cloud layer, between 2.5 and 8 km.

### (b) Specific impact of radiation

Figure 14 suggests that significant features occur, especially below 1 km, when radiation is included. Figure 15 shows the averaged differences of latent-heat budgets between the experiments which include radiative effects and the experiments which exclude them. A lowering of cloud base of about 300 m is induced by the radiation. The peak of diabatic heating, corresponding to an enhancement of convective activity at cloud base, is partly balanced by stronger convective transport of water vapour. A net drying up to 1 km is the result of these differences. This behaviour in the low layers is slightly more marked for simulations without large-scale ascent (not shown). A similar analysis which was done solely to find the effect of large-scale ascent revealed that this kind of forcing has no such impact at low levels.

Various mechanisms for the interaction between convection and radiation have been proposed in the past, and summarized recently by Fu *et al.* (1995). The first of these corresponds to a destabilization of the tropical atmosphere by clear-sky radiative cooling, leading to an enhancement of convection and hence to surface precipitation. A second mechanism involves horizontal differential radiative heating rates between the clear and

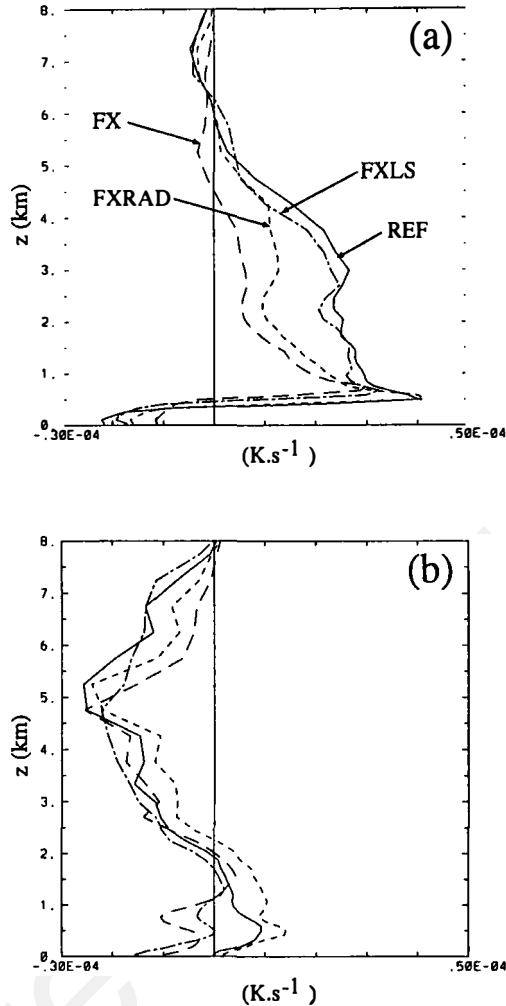


Figure 14. Vertical budgets averaged over the period 8 h to 48 h for experiments REF, FX, FXRAD and FXLS of: (a)  $\langle(L_v)/c_p\rangle\dot{Q}$ ; (b)  $-\langle(L_v)/c_p\rangle\partial q_v/\partial t$ .

cloudy areas (i.e. radiative properties of clouds), from which the resulting horizontal gradients can produce secondary circulations, and hence tend to enhance convection. A third mechanism depends on cloud-top cooling and cloud-base warming producing vertical gradients which destabilize the atmosphere. This mechanism mainly contributes to the longevity of anvil clouds.

In agreement with previous studies, our results suggest that radiation processes significantly increase convective activity. Nevertheless the present simulations concern a population of moderate precipitating clouds with weak large-scale ascent. In this case, the radiative processes appear to have a much stronger impact (precipitation increase of about 100% when large-scale ascent is zero) than for deep squall cloud clusters (precipitation increase of about 15%) as simulated by Fu *et al.* (1995) who showed that anvil clouds associated with squall clusters have a negative infrared radiative feedback because of their large extent (cloud fraction of about 50%). In our case, the cloud fraction is 5% in the

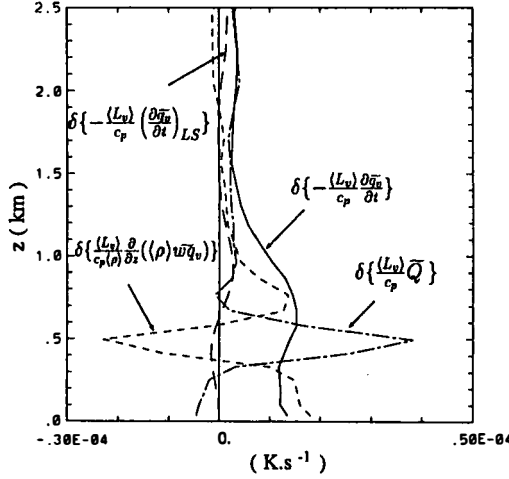


Figure 15. Averaged differences of latent-heat budgets between experiments including radiative effects and experiments excluding them for the layer 0.2 to 5 km and averaged over the period 8 h to 48 h.

period used in the budget analysis. This sensitivity of the radiative impact on the type and intensity of the convective system is consistent with our results, showing the decrease in radiative impact corresponding to an increasing large-scale ascent. The first two of the mechanisms noted above can provide an explanation for the observed impact. The present set of experiments however does not allow us to assess precisely the relative importance of each mechanism.

Due to radiation, there is also a significant increase of convective activity near the cloud base resulting in a lowering of the cloud base and a drying at low levels up to 1 km. The doubling, almost, of the cloud fraction at the cloud base indicates that there is an enhancement of shallow cumulus clouds (about 800 m thick). It is likely that the vertical destabilization via infrared radiative cloud-top cooling and cloud-base warming is an efficient mechanism for reinforcing small cumuli activity, and hence the transport vertically of water vapour. Fu *et al.* (1995) proposed a similar mechanism that led to more turbulence generation and increased the longevity and extent of anvil clouds associated with squall clusters. They also noted a significant increase of turbulence at low levels (see their Fig. 9(b)) due to this process, which reinforces our tentative explanation of the shallow convection intensification.

### (c) *Magnitude of the large-scale ascent*

Experiments HIGHLS 1 and HIGHLS 2 performed over 48 h differ from REF by the amplitude of the large-scale ascent,  $W_{LS}$ , twice and three times that used in REF, respectively. The time evolution of  $\tilde{q}_c(z, t)$  (Fig. 16) shows that, with larger overall convective activity, the cloud layer grows faster for both experiments than for REF. In the experiment HIGHLS 2, there is a change in the convective regime at about 32 h, similar to the one observed in REF at 48 h, with a violent convective event leading to a high cloud deck. The cumulative precipitations for experiments REF, HIGHLS 1 and HIGHLS 2 (Fig. 17) show that an increase in the large-scale introduction of cooler and moister air leads to an increase of the convective activity. In order to compare experiments HIGHLS 1 and HIGHLS 2 with REF, for similar convective conditions, the budgets are averaged over  $T'$  from 8 h to 32 h and integrated vertically over  $H'$  from zero to 9 km, since the cloud layer grew higher for HIGHLS 1 and HIGHLS 2 (Fig. 18).

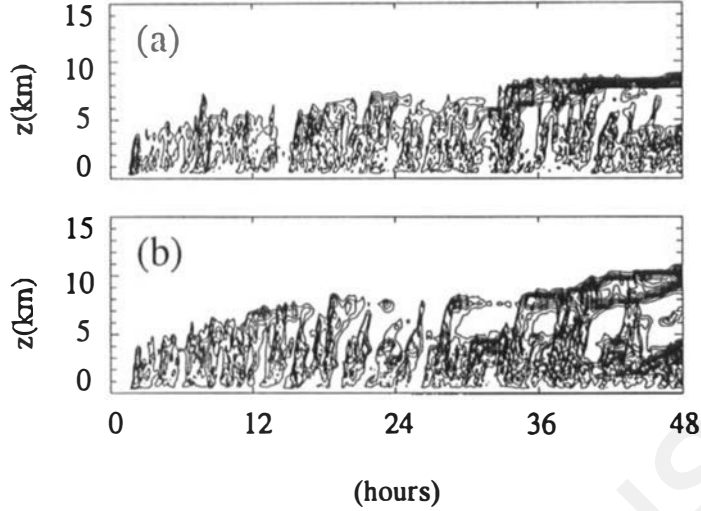


Figure 16. Same as for Fig. 5(a), but for experiments: (a) HIGHLS 1; (b) HIGHLS 2. Values of  $\tilde{q}_c$  are averaged over 10 min, with a contour interval of  $10^{-5}$ . The lower contour is  $10^{-5}$ ; the higher contours are  $13 \times 10^{-5}$  for HIGHLS 1 and  $17 \times 10^{-5}$  for HIGHLS 2.

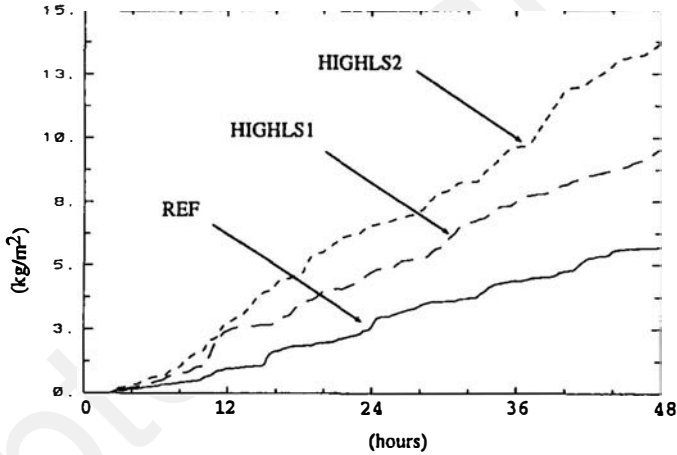


Figure 17. Same as for Fig. 12, but for experiments REF, HIGHLS 1 and HIGHLS 2.

Before looking at the budgets for heat,  $\bar{s}$ , and moisture,  $\overline{\langle L_v \rangle q_v}$ , let us consider the budget for moist static energy,  $\bar{h}$ . Whereas this quantity is in quasi-equilibrium for the REF experiment ( $\partial \bar{h} / \partial t = 2 \text{ W m}^{-2}$ ), the balance is disturbed when the large-scale ascent is increased ( $\partial \bar{h} / \partial t = 33$  and  $51 \text{ W m}^{-2}$  for HIGHLS 1 and HIGHLS 2, respectively). For HIGHLS 1, the increase in  $\overline{\langle L_v \rangle Q}$  is such that the resulting storage of water is less important than for REF. For HIGHLS 2, although  $\overline{\langle L_v \rangle Q}$  still increases, the water storage increases. This enhancement is located firstly at the levels to which the cooler and moister air is brought by the large-scale ascent, and then above 5 km, since the mean cloud top is higher (Fig. 19(a)). As for FX, FXRAD and FXLS, the structure of the water vapour storage is similar and located above 2 km, with a maximum in the upper part of the cloud layer.

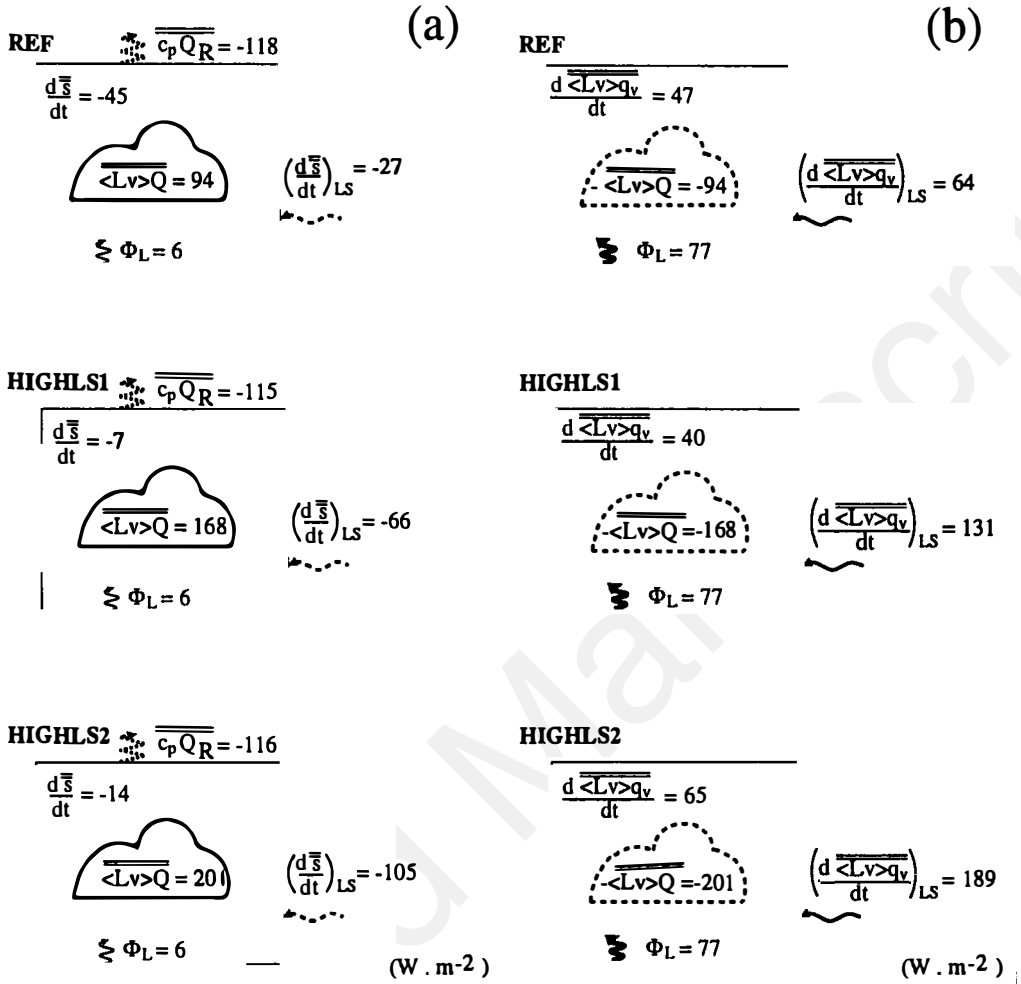


Figure 18. OD budgets of: (a)  $\bar{s}$ ; (b)  $\langle Lv \rangle q_v$ , averaged over the period 8 h to 32 h for experiments HIGHLS 1 and HIGHLS 2.

This sensitivity study confirms the strong modulation of convection by large-scale advective processes, as already reported by Krueger (1988) and Xu *et al.* (1992) using forcings much stronger than were used by us.

## 6. DIURNAL CYCLE

In the previous section, we noted that convection was enhanced by radiative effects. In this section, we examine whether the diurnal cycle influences convection. Over an open ocean, evidence of a diurnal cycle in convection is weaker than over land. Nevertheless, observations of cloudiness and precipitation rates show clearly the existence of a diurnal cycle in oceanic convection (Gray and Jacobson 1977; McBride and Gray 1980). Recently Negri *et al.* (1994) examined the diurnal variation of regional rainfall derived from the

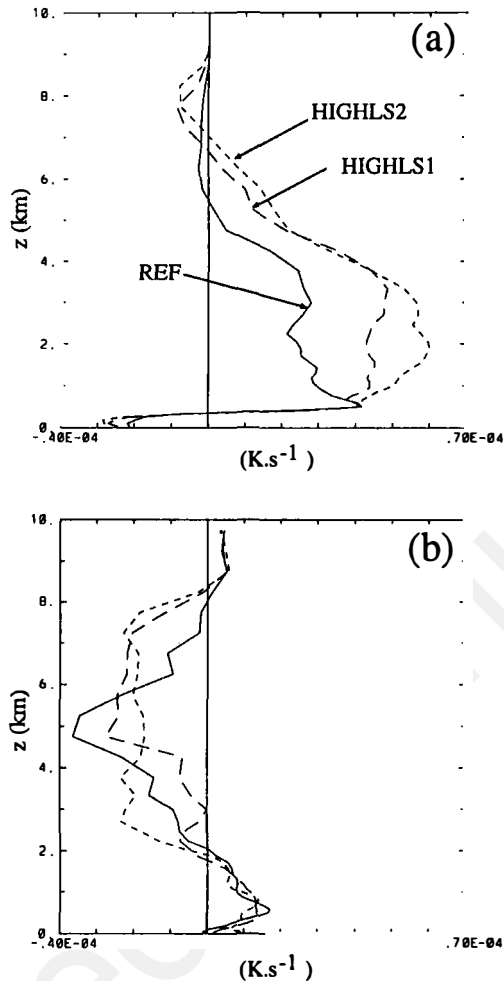


Figure 19. Same as for Fig. 14, but averaged over the period 8 h to 32 h and for experiments HIGHLS 1 and HIGHLS 2.

special sensor microwave imager (SSM/I) data. For instance, over the region of the west Pacific (as observed during the IOP of TOGA COARE), there is a clear preference for morning precipitation away from the effects of major land masses. The diurnal cycle characteristics seem to be dependent on whatever ocean basin is considered; and, up to now, the physical bases of this cycle have not been well established. However, the diurnal cycle appears as an important factor influencing the radiative cloud forcing (cloud radiative effects are quite different by night and day) and modulating the precipitation cycle.

Several experiments have been performed with and without a diurnal cycle of radiation, for differing values of surface fluxes and large-scale ascent. The results of three of them, including the radiative diurnal cycle, CYCLE, CYCLE 1 and CYCLE 2, are presented here (see Table 1). The experiment CYCLE is analogous to REF except for the addition of the diurnal cycle (initial time is 4.00 pm local time). The experiments CYCLE 1 and CYCLE 2 differ from CYCLE by having different surface fluxes of sensible heat (5 and 10  $\text{W m}^{-2}$ ) and latent heat (50 and 100  $\text{W m}^{-2}$ ).

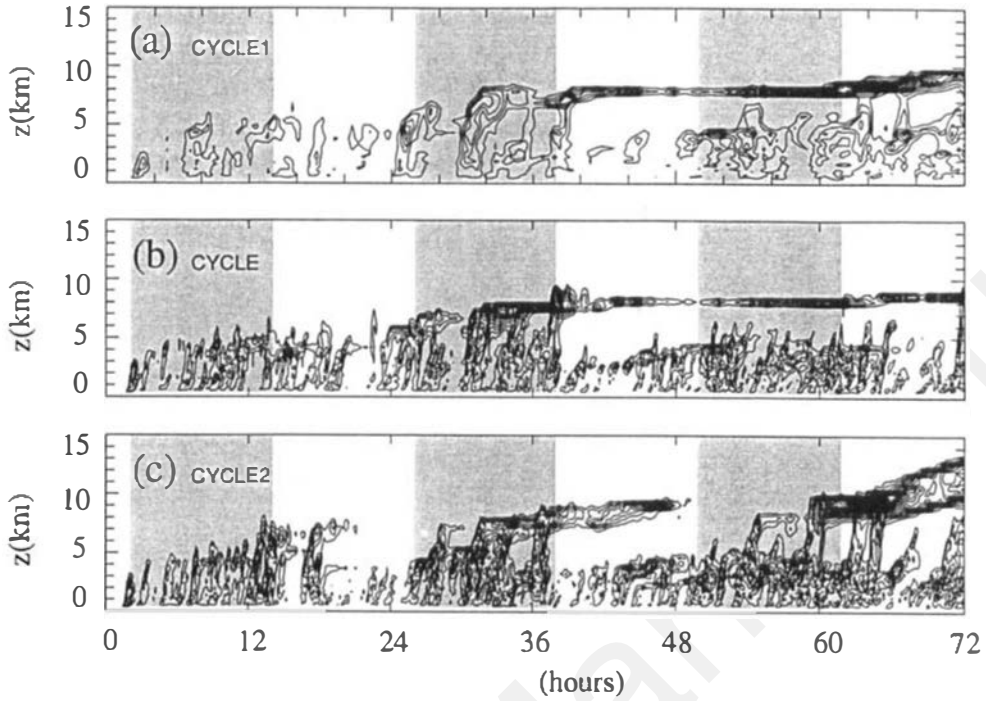


Figure 20. Same as for Fig. 5(a) but for experiments: (a) CYCLE 1; (B) CYCLE; (c) CYCLE 2 (contour interval of  $10^{-5}$ ); the lower contour is  $10^{-5}$  and the higher contours are  $15 \times 10^{-5}$  for CYCLE 1,  $14 \times 10^{-5}$  for CYCLE and  $25 \times 10^{-5}$  for CYCLE 2. Grey corresponds to night-time.

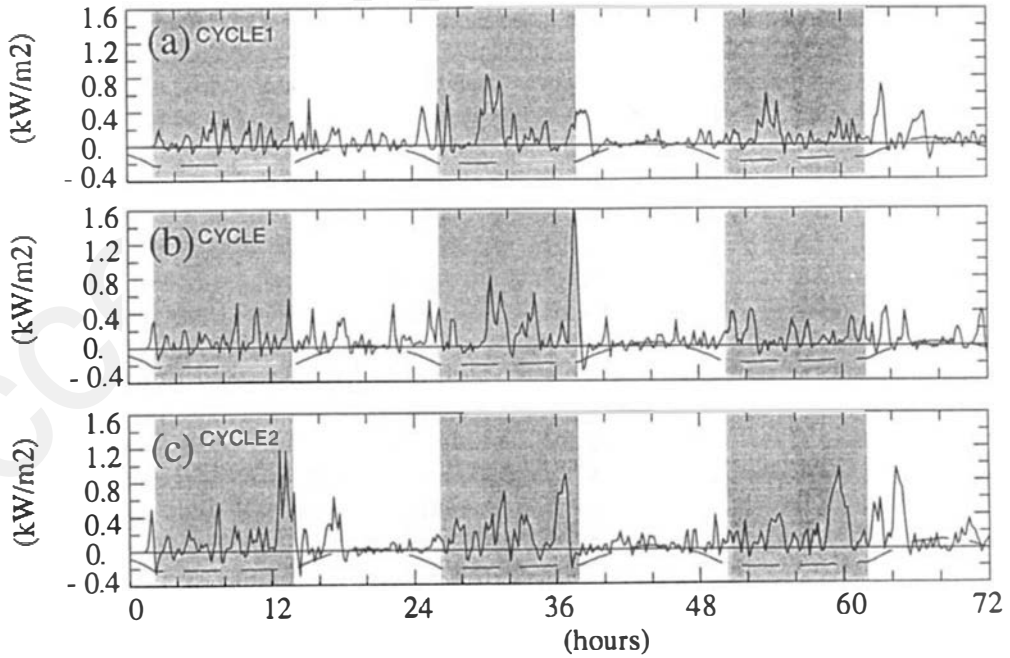


Figure 21. Evolution with time of  $\overline{\langle L_v \rangle Q}$  and  $\overline{c_p Q_R}$  for experiments (a) CYCLE 1; (b) CYCLE; (c) CYCLE 2.

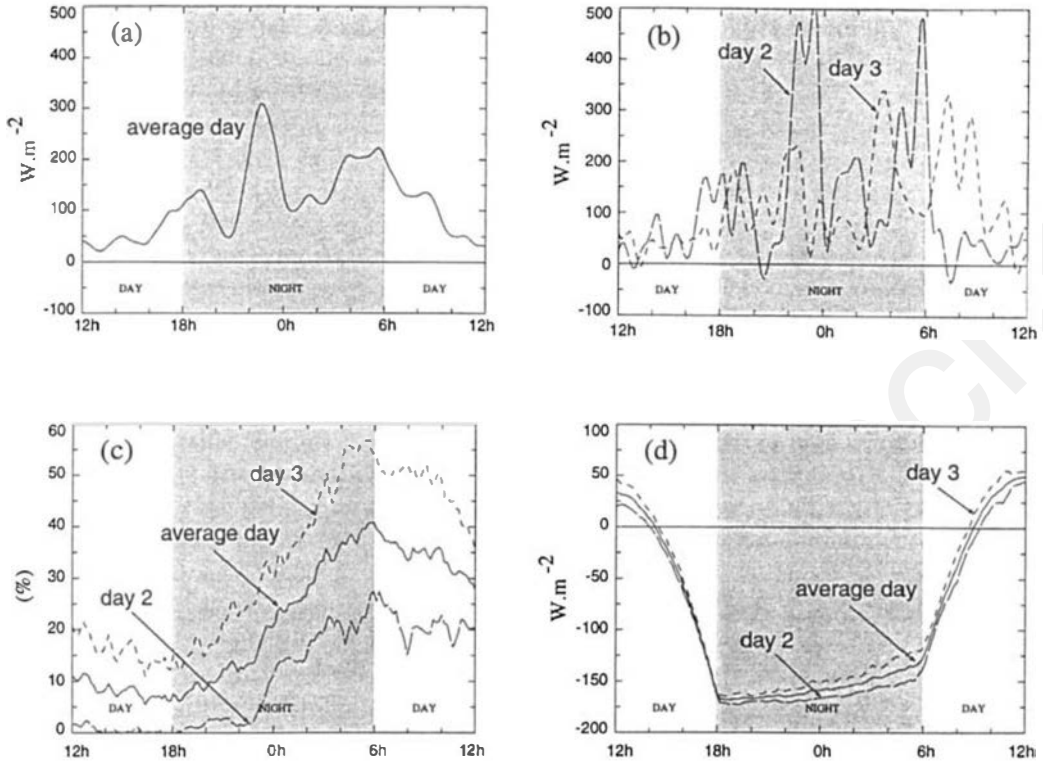


Figure 22. Diurnal evolution for experiments CYCLE 1, CYCLE and CYCLE 2 of  $\overline{\langle L_v \rangle Q}$  (low-pass filter of 80 min): (a) averaged over the two last days; (b) over the 2nd and 3rd days, and of (c) the maximum cloud fraction above 7 km; (d) the net radiative heating over the layer 0 to 8 km for the same periods.

Figures 20 and 21 give a general idea of how convection varies with time when the diurnal cycle is included. It will be noticed that the introduction of radiation causes a time modulation of convection (compare Figs. 5(a) and (c) with Figs. 20(b) and 21(b)). In particular, for CYCLE, a strong convective event occurs after about 30 hours of simulation, during the second night, instead of after 48 hours as in experiment REF. A high cloud deck then remains until the end of the second day, at which time, after 50 hours of simulation, it almost disappears. As opposed to CYCLE, experiment CYCLE 2 (Figs. 20(c) and 21(c)), with larger surface fluxes, shows a more marked diurnal cycle of convection, with peaks of convective activity occurring during the night or in the early morning. As previously noted for CYCLE, convective activity is reduced around midday. When the surface fluxes are reduced (experiment CYCLE 1) convective activity is less intense but it still has a diurnal cycle, with maximum activity during the night and in the morning (after the first day).

By way of analysing the diurnal cycle clearly, Fig. 22 shows the evolution of two significant parameters (net latent heat release and cloud cover at upper levels) for the final two days of the experiments CYCLE, CYCLE 1 and CYCLE 2. A low-pass filter (80 minutes) is used to remove the strong and rapid time fluctuations due to convective cells. The first day of the simulation has not been taken into consideration in this analysis since it corresponds to a spin-up phase related to the initialization mode. In addition to the differences between experiments noted above, Fig. 22(a) clearly exhibits the strong diurnal modulation of the convective activity as measured by the total diabatic heating.

The strongest activity occurs during the night (mean value of  $160 \text{ W m}^{-2}$  from 18 h to 6 h), whereas during the day activity is reduced (mean value of  $77 \text{ W m}^{-2}$  from 6 h to 18 h). Minimum activity is noticed around midday and early afternoon, whereas maxima occur frequently around midnight and at the end of the night. Systematic differences appear, nevertheless, between the second and third days (Fig. 22(b)). In particular the convective activity reaches its maximum later during the last night, and the secondary morning maximum occurs later on the third day. The net radiative cooling (Fig. 22(d)) in the cloud layer is maximum during the night, whereas constant sea surface temperature maintains the subcloud energy. The resulting effect is a destabilization which is maximum at night. However, this does not directly explain the difference in behaviour observed between the second and third days.

This intense diurnal cycle can also be seen in other parameters such as the fraction of sky covered by anvil clouds (above 7 km) (Fig. 22(c)). The magnitude of this oscillation reaches 35% on average. The anvil deck reaches its maximum extent at sunrise and its minimum at sunset, which corresponds to a phase lag of 6 hours (i.e. a quarter of a period) with the convective activity curve. There are three mechanisms that might contribute to this cycle. First, the anvil formation by the deepest convection, occurring during the night, is certainly the main factor responsible for the sunset absolute maximum. Figure 20 illustrates the occurrence of such events, for instance between 30 h and 36 h of experiment CYCLE 2. Secondly, the vertical destabilization by infrared radiative cooling from the top and warming at the base contributes to the longevity and extent of anvils, as has been shown by Fu *et al.* (1995). Thirdly, the dissipation of anvil clouds is strongest during the day, owing to the solar radiation stabilizing this thin cloud layer by warming at the top. For instance, after the anvil formation by deep convection on the second night of simulation CYCLE (Fig. 20(a)), all the anvil dissipates during the following day. Just after sunset the anvil deck increases, whereas deep convection has not yet started.

Beside the basic cycle affecting the anvil cloud deck, its horizontal extent increases during the simulation (20% more on day 3 than on day 2), to reach a cloud fraction of up to 50% on the last morning. This extent is sufficiently large on the third day to suggest that the anvil cloud has a major radiative impact on the simulated atmosphere. The anvil clouds decrease the infrared radiative cooling and warm the troposphere at the same time, leading to a negative feedback on convection (as indicated in Fig. 22(d)). The anvil cloud radiative feedback, recently discussed by Fu *et al.* (1995), seems to explain most of the modulation observed in this simulated diurnal cycle. The larger anvil deck during the third day contributes to a weaker diurnal cycle on that day. The convection maximum occurs later in the night, and in the morning rather than on the previous night. This may be partly due to a wider anvil cloud deck which reduces the convective development, through the stronger negative feedback of the anvil cloud.

In summary, for experiments performed with the weak large-scale ascent (the same as REF), the time evolution of the convective activity shows a diurnal cycle, with a preference for the occurrence of active convection during the night and weak convection around midday. Xu *et al.* (1995) found, qualitatively, the same features in their explicit simulation of a cloud ensemble.

However, experiments with stronger large-scale ascent did not present these features. Convection maxima appear rather sporadically during the day and the night for these cases without a strong convective activity, and after three days of simulation. The weak convective activity is, possibly, responsible for the difference from the results of Xu *et al.* (1995) who obtained a diurnal cycle of convective activity for the case with strong large-scale ascent.

## 7. CONCLUSION

In this study, the behaviour of a population of tropical moderate precipitating clouds has been investigated with a cloud-resolving model over a period of two to three days. The response of the system to given external forcings, including shortwave and longwave radiation, large-scale flow effects and surface fluxes, has been analysed using thermodynamic budgets averaged over periods of one to two days.

In the control simulation the moist static energy is approximately in equilibrium. Its sources however are not redistributed by convection to keep steady the domain-averaged dry static energy and water vapour. In fact, the atmosphere cools and moistens. The convective activity condenses about two thirds of the introduced water vapour, the other third is stored in and above the cloud layer. The vapour storage is driven by the vertical transport, convection continuously bringing water vapour upwards. The convective transport leads to a decoupling between the vertical distribution of dry static energy and water vapour. Consequently the vertical distribution of the apparent moisture sink,  $Q_2$ , behaves differently above 2 km from that of the apparent heat source,  $Q_1 - \bar{Q}_R$ . For all the sensitivity experiments performed, the shape of the vertical redistribution of water vapour presented similar features, with a storage of vapour in the higher part of the cloud layer and in the region above. A large-scale mechanism at this higher level would be required to balance this storage. In the context of the study of radiative-convective equilibrium, based on cloud-resolving models, this could be critical. Large-scale horizontal advection (not included in this study) though weaker than vertical advection, can weaken this vapour storage process. This is a point which needs to be investigated further. A storage phenomenon of this kind has already been noticed by Gregory and Miller (1989) and by Lipps and Hemler (1986) in simulations and observations of cases of deep convection.

In all experiments, for time averages of a few hours, the budgets for cloud and rain water content are reasonably well balanced. In consequence, the net condensation and precipitation rates have always similar magnitudes.

The sensitivity of convective activity to external forcings has been investigated. Radiative processes enhance the convective activity, especially in the absence of large-scale vertical ascent. The most noticeable effects of radiation are a lowering of the cloud base and indirect drying in the low layers. In effect, the increase of cloud activity is a maximum above the PBL and enhances the transport of humidity from the PBL to the free troposphere, resulting in a drying of the lower troposphere.

The entrainment of cooler and moister air due to large-scale ascent also enhances the convective activity. Part of the moisture in this air is condensed through moist convective processes. The net impact of large-scale ascent consists in a moistening of the system, but without significant cooling owing to an associated increase in convective activity. The convective response increases when the magnitude of the imposed large-scale ascent increases. The water storage also increases, located at those levels to which the cooler and moister air is transported by the large-scale ascent, and above 5 km, since the mean cloud top is higher.

When considering the diurnal cycle in the radiative processes, a modulation of the cloud activity is obtained for those experiments with moderate large-scale ascent. For those cases, convection is more intense during the night and in the morning. The diurnal cycle of the convective activity may be explained by the strong diurnal cycle of the net radiative cooling. An increase of anvil cloud extent (proportional cloud cover up to 50% during the third day) during the simulation leads to a different diurnal cycle during the second and third days, through an infrared radiative feedback. Due to a larger anvil cloud deck during the third day, the convection maximum occurs later in the night and in the morning rather

than during the second day. A modulation of anvil cloud fraction with the diurnal cycle of radiation is also obtained, but with a phase lag of 6 hours compared with the convection cycle.

#### ACKNOWLEDGEMENTS

The authors are grateful to J. J. Morcrette for providing the radiation model and to N. Asencio for very helpful computing assistance. The text was improved by the changes suggested by D. Stephenson and journal reviewers who provided valuable comments and suggestions, particularly as regards the understanding of convective diurnal variations.

#### APPENDIX A

##### *The radiation model*

The radiation model includes a treatment of both longwave and shortwave radiative processes. For shortwave, it is based on a two-stream formulation used with a photon path distribution method having two spectral intervals: 0.25–0.68  $\mu\text{m}$  and 0.68–4  $\mu\text{m}$ . For longwave, a broad-band flux emissivity method is used with six spectral bands between 0 and 2620  $\text{cm}^{-1}$  (for a detailed description of this model see Morcrette 1991).

For shortwave, the optical thickness,  $\tau$ , of a cloud layer is expressed in the form

$$\tau = \tau_c + \tau_r = \frac{3}{2} \left( \frac{LWP_c}{Re_c} + \frac{LWP_r}{Re_r} \right)$$

where  $LWP_c$  ( $LWP_r$ ) and  $Re_c$  ( $Re_r$ ) are, respectively, the liquid water path of cloud droplets (raindrops) and the mean effective radius size of the distribution of cloud droplets (raindrops).  $Re_c$  is set to 15  $\mu\text{m}$ . As the distribution of raindrops in the cloud-resolving model follows a Marshall–Palmer law (Redelsperger and Sommeria 1986),  $Re_r$  is a linear function of  $q_r^{0.25}$ , where  $q_r$  is the rain water content predicted in the cloud model. Values of  $Re_r$  range between 100 and 1000  $\mu\text{m}$ ; consequently  $\tau_r \ll \tau_c$ .

For longwave, clouds are considered as grey bodies with an emissivity,  $\epsilon$ , expressed as

$$\epsilon = 1 - \exp(-0.158LWP_c)$$

Figure A.1 gives one example of a computed radiative divergence in both the longwave and shortwave ranges (at 12 h, when the shortwave radiative divergence is maximum) for a simulated cloud ensemble. The predicted radiative fluxes are strongly correlated with the cloud field, presenting large gradients at the top of the clouds, with rates of longwave cooling and shortwave heating of several tens of degrees Kelvin per hour. The longwave radiation also heats the bottom of the clouds at rates of several degrees Kelvin per hour.

The introduction of radiative effects in a cloud model causes an important increase in the computational cost, even with a vectorized radiation code. For the simulations presented in this paper, radiative effects are computed for each column, every 16 min for clear sky conditions, and every 4 min in the presence of a cloud layer. Tests lasting over one hour show negligible differences between the budgets, with a computation made every 30 s and every 4 min in cloudy conditions. The increase of cloud model CPU time due to the inclusion of radiation is 90% and 40% in the case of a computation for cloudy conditions every 30 s and every 4 min, respectively.

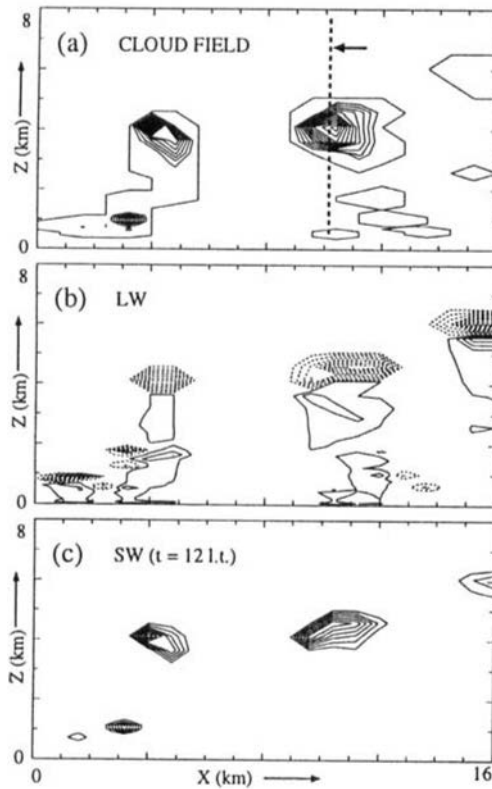


Figure A.1. Vertical cross-section in part of the domain of: (a)  $q_c$  at  $1.5 \times 10^{-4} \text{ kg kg}^{-1}$  intervals, lower and higher contours are  $0 \text{ kg kg}^{-1}$  and  $2.1 \times 10^{-3} \text{ kg kg}^{-1}$ , respectively; (b) longwave radiative flux divergence at  $5 \text{ K d}^{-1}$  intervals, lower and higher contours are  $-50 \text{ K d}^{-1}$  and  $15 \text{ K d}^{-1}$ , respectively; (c) shortwave radiative flux divergence at  $5 \text{ K d}^{-1}$  intervals, lower and higher contours are  $0 \text{ K d}^{-1}$  and  $40 \text{ K d}^{-1}$ , respectively.

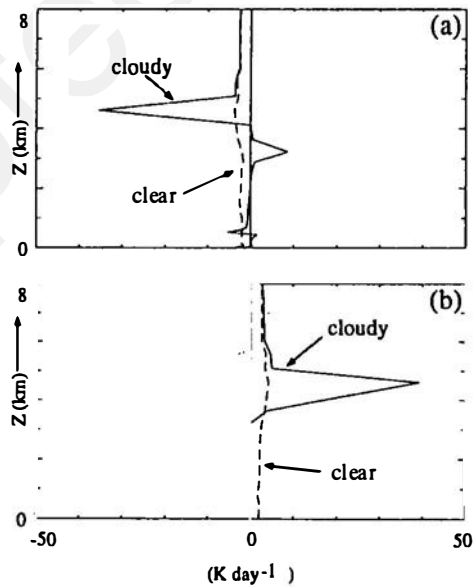


Figure A.2. Vertical profiles of the divergence of: (a) longwave and (b) shortwave radiative fluxes in clear and cloudy conditions for the vertical cross-section indicated in Fig. A.1.

## REFERENCES

- Arakawa, A. and Schubert, W. H. 1974 Interaction of a cumulus cloud ensemble with the large-scale environment, Part I. *J. Atmos. Sci.*, **31**, 674–701
- Arking, A. 1991 The radiative effects of clouds and their impact on climate. *Bull. Am. Meteorol. Soc.*, **72**, 795–831
- Balaji, V., Redelsperger, J.-L. and Klaassen, G. P. 1993 Mechanisms for the mesoscale organisation of tropical cloud clusters in GATE phase III. Part I: shallow cloud bands. *J. Atmos. Sci.*, **50**, 3571–3589
- Betts, A. K. and Ridgway, W. 1989 Climatic equilibrium of the atmospheric convective boundary layer over a tropical ocean. *J. Atmos. Sci.*, **46**, 2622–2641
- Browning, K. A. and G.E.W.E.X Cloud System Study Team 1993 The GEWEX cloud system study (GCSS). *Bull. Am. Meteorol. Soc.*, **74**, 387–399
- Caniaux, G., Redelsperger, J.-L. and Lafore, J.-P. 1994 A numerical study of the stratiform region of a fast-moving squall line. Part I: general description and water and heat budgets. *J. Atmos. Sci.*, **51**, 2046–2074
- Cess, R. D., Potter, G. L., Blanchet, J. P., Boer, G. J., Del Genio, A. D., Deque, M., Dymnikov, V., Galin, V., Gates, W. L., Ghan, S. J., Kiehl, J. T., Lacis, A. A., Le Treut, H., Li, Z.-X., Liang, X.-Z., McAvaney, B. J., Meleshko, V. P., Mitchell, J. F. B., Morcrette, J.-J., Randall, D. A., Rikus, L., Roeckner, E., Royer, J. F., Schlese, U., Sheinin, D. A., Slingo, A., Sokolov, A. P., Taylor, K. E., Washington, W. M., Wetheral, R. T., Yagai, I. and Zhang, M.-H. 1990 Intercomparison and interpretation of climate feedback processes in 19 atmospheric general circulation models. *J. Geophys. Res.*, **95**, 16601–16615
- Chong, M. and Hauser, D. 1989 A tropical squall line observed during the COPT 81 experiment in West Africa. Part III: heat and moisture budgets. *Mon. Weather Rev.*, **117**, 728–744
- Emanuel, K. A. and Raymond, D. J. 1993 *The representation of cumulus convection in numerical models*, vol. 24. American Meteorological Society
- Frank, W. M. 1978 The life cycles of gate convective systems. *J. Atmos. Sci.*, **35**, 1256–1264
- Fu, Q., Krueger, S. K. and Liou, K. N. 1995 Interactions of radiation and convection in simulated tropical cloud clusters. *J. Atmos. Sci.*, **52**, 1310–1328
- Gray, W. M. and Jacobson Jr., R. W. 1977 Diurnal variation of deep cumulus convection. *Mon. Weather Rev.*, **105**, 1171–1188
- Gregory, D. and Miller, M. J. 1989 A numerical study of the parametrization of deep tropical convection. *Q. J. R. Meteorol. Soc.*, **115**, 1209–1241
- Held, I. M., Hemler, R. S. and Ramaswamy, V. 1993 Radiative-convective equilibrium with explicit two-dimensional moist convection. *J. Atmos. Sci.*, **50**, 3909–3927
- Hu, Q. and Randall, A. 1994 Low-frequency oscillations in radiative-convective systems. *J. Atmos. Sci.*, **51**, 1089–1099
- Johnson, R. H. 1984 Partitioning tropical heat and moisture budgets into cumulus and mesoscale components: implications for cumulus parameterization. *Mon. Weather Rev.*, **112**, 1590–1601
- Krueger, S. K. 1988 Numerical simulation of tropical cumulus clouds and their interactions with the subcloud layer. *J. Atmos. Sci.*, **45**, 2221–2250
- Kuo, H. L. 1974 Further studies of the parameterisation of the influence of cumulus convection of large-scale flow. *J. Atmos. Sci.*, **31**, 1232–1240
- Lafore, J.-P. and Redelsperger, J.-L. 1992 Effects of convection on mass and momentum fields as seen from cloud scale simulations of precipitating systems. *Proc. Workshop on fine-scale modelling and the development of parametrization schemes, 16–18 Sept. 1991*. European Centre for Medium-Range Weather Forecasts
- Lafore, J.-P., Redelsperger, J.-L. and Jaubert, G. 1988 Comparison between a three-dimensional simulation and doppler radar data of a tropical squall line: transport of mass, momentum, heat and moisture. *J. Atmos. Sci.*, **45**, 3483–3500

- Lau, K.-M., Sui, C.-H. and Tao, W.-K. 1993 A preliminary study of the tropical water cycle and its sensitivity to surface warming. *Bull. Am. Meteorol. Soc.*, **74**, 1313–1321
- Lau, K.-M., Sui, C.-H., Chou, M.-D. and Tao, W.-K. 1994 An inquiry into the cirrus-cloud thermostat effect for tropical sea surface temperature. *Geophys. Res. Lett.*, **21**, 1157–1160
- Leary, C. A. and Houze, R. A. 1980 The contribution of mesoscale motions to the mass and heat fluxes of an intense tropical convective system. *J. Atmos. Sci.*, **37**, 784–796
- Lipps, F. B. and Hemler, R. S. 1986 Numerical simulation of deep tropical convection associated with large-scale convergence. *J. Atmos. Sci.*, **43**, 1796–1816
- Lord, S. J. 1982 Interaction of cumulus cloud ensemble with the large-scale environment. Part III: Semi-prognostic test of the Arakawa–Schubert cumulus parameterization. *J. Atmos. Sci.*, **39**, 88–103
- Louis, J. F. 1979 A parametric model of vertical eddy fluxes in the atmosphere. *Boundary-Layer Meteorol.*, **17**, 187–202
- McBride, J. L. and Gray, W. M. 1980 Mass divergence in tropical weather systems—Paper I: diurnal variation. *Q. J. R. Meteorol. Soc.*, **106**, 501–516
- Miller, R. A. and Frank, W. M. 1993 Radiative forcing of simulated tropical cloud clusters. *Mon. Weather Rev.*, **121**, 482–498
- Morcrette, J.-J. 1991 Radiation and cloud radiative properties in the European Centre for Medium-Range Weather Forecasts forecasting system. *J. Geophys. Res.*, **96**, 9121–9132
- Negri, A. J., Adler, R. F., Nelkin, E. J. and Huffman, G. J. 1994 Regional rainfall climatologies derived from special sensor microwave imager (SSM/I) data. *Bull. Am. Meteorol. Soc.*, **75**, 1165–1182
- Redelsperger, J.-L. and Clark, T. L. 1990 The initiation and horizontal scale selection of convection over gently sloping terrain. *J. Atmos. Sci.*, **47**, 516–541
- Redelsperger, J.-L. and Lafore, J.-P. 1988 A three-dimensional simulation of a tropical squall line: Convective organisation and thermodynamical transport. *J. Atmos. Sci.*, **45**, 1334–1356
- 1994 Non-hydrostatic simulations of a cold front observed during the FRONT 87 experiment. *Q. J. R. Meteorol. Soc.*, **120**, 519–555
- Redelsperger, J.-L. and Sommeria, G. 1986 Three-dimensional simulation of a convective storm: Sensitivity studies on subgrid parameterisation and spatial resolution. *J. Atmos. Sci.*, **43**, 2619–2635
- Satoh, M. and Hayashi, Y.-Y. 1992 Simple cumulus models in one-dimensional radiative convective equilibrium problems. *J. Atmos. Sci.*, **49**, 1202–1220
- Sommeria, G. 1976 Three-dimensional simulation of turbulent processes in an undisturbed tradewind boundary layer. *J. Atmos. Sci.*, **33**, 216–241
- Soong, S.-T. and Ogura, Y. 1980 Response of tradewind cumuli to large-scale processes. *J. Atmos. Sci.*, **37**, 2035–2050
- Soong, S.-T. and Tao, W.-K. 1980 Response of deep tropical cumulus clouds to mesoscale processes. *J. Atmos. Sci.*, **37**, 2016–2034
- Sui, C.-H., Lau, K. M., Tao, W.-K. and Simpson, J. 1994 The tropical water and energy cycles in a cumulus ensemble model. Part I: Equilibrium climate. *J. Atmos. Sci.*, **51**, 711–728
- Tao, W.-K. and Soong, S.-T. 1986 A study of the response of deep tropical cumulus clouds to mesoscale processes: Three-dimensional numerical experiments. *J. Atmos. Sci.*, **43**, 2653–2676
- Tao, W.-K., Simpson, J., Sui, C.-H., Ferrier, B., Lang, S., Scala, J., Chou, M.-D. and Pickering, K. 1993 Heating, moisture, and water budgets of tropical and midlatitude squall lines: Comparisons and sensitivity to longwave radiation. *J. Atmos. Sci.*, **50**, 673–690
- Wong, T., Stephens Jr., G. L., Stackhouse, P. W. and Valero, P. J. 1993 The radiative budgets of a tropical mesoscale convective cloud system during the emex-step-amex experiment. *J. Geophys. Res.*, **98**, 8695–8711
- Xu K.-M. and Arakawa, A. 1992 Semiprognostic tests of the Arakawa–Schubert cumulus parameterization using simulated data. *J. Atmos. Sci.*, **49**, 2421–2436
- Xu, K.-M., Arakawa, A. and Krueger, S. K. 1992 The macroscopic behavior of cumulus ensembles simulated by a cumulus ensemble model. *J. Atmos. Sci.*, **49**, 2402–2420
- Xu, K.-M. and Randall, D. A. 1995 Impact of interactive transfer on the macroscopic behavior of cumulus ensembles. Part II: Mechanisms for cloud-radiation interactions. *J. Atmos. Sci.*, **52**, 800–817
- Yanai, M., Esbensen, S. and Chu, J.-H. 1973 Determination of bulk properties of tropical cloud clusters from large-scale heat and moisture budgets. *J. Atmos. Sci.*, **30**, 611–627